Check for updates

PLANETARY SCIENCE

Cassini CDA observes compositional segregation of Enceladus' ice grains from slow freezing and fragmentation of oceanic spray

Frank Postberg[1]*†, Zenghui Zou[1,2]†, Yasuhito Sekine[3,4,5], Minori Koga[3], Jürgen Schmidt[1], Mark Fox-Powell[6], Fabian Klenner[7,8], Jon K. Hillier[1], Nozair Khawaja[1], Toshihiko Kadono[9], Melih Çakar[1,3], Sascha Kempf[10], Ralf Srama[11]

Copyright © 2026 The Authors, some rights reserved; exclusive licensee American Association for the Advancement of Science. No claim to original U.S. Government Works. Distributed under a Creative Commons Attribution NonCommercial License 4.0 (CC BY-NC).

Salt-rich ice particles, termed Type 3, are a major compositional group within Enceladus' plume and Saturn's E ring and are thought to represent frozen micrometer-sized aerosolized droplets of Enceladus' salty subsurface ocean. Here, we present an analysis on the basis of ≈1000 mass spectra of individual Type 3 E ring ice grains recorded by Cassini's Cosmic Dust Analyzer (CDA), revealing a large compositional diversity among these grains. We find at least five basic compositional subtypes dominated by either sodium chloride (NaCl), sodium bicarbonate ($NaHCO_3$)/sodium carbonate (Na_2CO_3), disodium phosphate (Na_2HPO_4)/trisodium phosphate (Na_3PO_4), sodium hydroxide (NaOH), potassium chloride (KCl), or potassium hydroxide (KOH). By conducting experiments and thermodynamic calculations, we show that salt separation in agreement with CDA observations occurs as a consequence of salt mineral precipitation only within droplet sizes >10 micrometers and freezing rates below 20 kelvins per minute. We suggest that oceanic spray forms with an average size of 100s of micrometers entrained in a slow gas flow, causing slow freezing and separation of salts. Subsequently, they are accelerated to speeds >100 meters per second in narrow ice vents where frequent wall collisions lead to much smaller fragments mostly containing a single type of salt, matching CDA observations. The gradual cooling of ocean droplets in combination with wall collisions determines the final size distribution and provides an efficient chemical separation of both inorganic and organic oceanic constituents into differently composed ice grains ejected into Enceladus' plume.

INTRODUCTION

Enceladus' global ocean lies under an ice crust and above a rocky core where tidal dissipation (*1*, *2*) is suspected to drive hydrothermal activity (*3*, *4*). By cryovolcanic activity, the moon ejects icy particles into Saturn's E ring (*5*), which therefore is composed of micrometer- and submicrometer-sized icy dust particles (*6*–*8*) that are sourced from Enceladus' subsurface ocean (*9*). From 2004 until 2017, the Cosmic Dust Analyzer (CDA) aboard the Cassini-Huygens spacecraft recorded the individual compositions of these ice grains with its impact ionization mass spectrometer. The analysis of E ring grains by the CDA provides important insights into the composition of the subsurface ocean, with much better statistics compared to data from the rare and short occasions when Cassini traversed the plume.

Previous analysis of CDA E ring spectra classified these ice grains into three basic compositional groups (*9*, *10*): Type 1 ice grains are almost pure water ice grains and show spectral features corresponding to water and sub–parts per million (ppm) amounts of sodium salts. Type 2 ice grains show spectral features corresponding to organics in these grains, and Type3 ice grains are salt-rich ice grains indicating markedly increased salinity (in the order of 1% by mass) with respect to Types 1 and 2 [ppm-level salinity or less (*9*)]. Subsequent analysis further classified Type 2 grains into subcategories, containing volatile, aromatic, and N- and O-bearing species (*11*, *12*) as well as hydrophobic macromolecular compounds (*13*).

This work focuses on the composition of the salt-rich Type 3 E ring ice grains. In general, Type 3 grains are thought to originate from frozen aerosolized droplets, dispersed from the salty seawater of the subsurface ocean of Enceladus by the bursting of bubbles (*9*, *13*–*15*). Thus, they are assumed to reflect the composition of the ocean water (*9*) and help assess subsurface geochemical processes, such as water-rock interactions within the moon (*9*, *14*, *16*, *17*). Previous work (*9*) used the average composition of spectra from 105 individual Type 3 E ring grains to assess the composition of the ocean. It was found that sodium (Na^+) and chloride (Cl^-) are expected to be the most abundant components dissolved in the ocean, followed by substantial amounts of bicarbonate (HCO_3^-) and/or carbonate (CO_3^{2-}), indistinguishable by the CDA. Traces of potassium K^+ had been identified, too. More recently, a reanalysis of a larger CDA E ring dataset additionally found that both monohydrogenphosphate (HPO_4^{2-}) and phosphate (PO_4^{3-}) are present in substantial quantities in the order of a few millimole (*16*).

Paper outline and goals of this work

In this work, we use the same dataset as in (*16*) and examine 961 individual Type 3 E ring spectra (see the "CDA analysis of compositional variation in the population of salt-rich ice grains" section), typically ranging from 0.4 to 4 μm in diameter. In contrast to the previous Type 3 analyses in (*9*), this work does not focus on the inference of the average composition but aims to assess the compositional

[1]Institute of Geological Sciences, Freie Universität Berlin, Berlin, Germany. [2]School of Mathematics and Physics, Qinghai University, Xining, China. [3]Earth-Life Science Institute (ELSI), Tokyo Institute of Technology, Tokyo, Japan. [4]GENTEN Research Center, Institute of Science Tokyo, Tokyo, Japan. [5]Institute of Nature and Environmental Technology, Kanazawa University, Kanazawa, Japan. [6]School of Environment, Earth & Ecosystem Sciences, The Open University, Milton-Keynes, UK. [7]Department of Earth and Space Sciences, University of Washington, Seattle, WA 98195, USA. [8]Department of Earth and Planetary Sciences, University of California, Riverside, CA 92521, USA. [9]Department of Basic Sciences, University of Occupational and Environmental Health, Kitakyushu, Japan. [10]Laboratory for Atmospheric and Space Physics, University of Colorado in Boulder, Boulder, CO 80303, USA. [11]Institut für Raumfahrtsysteme, Universität Stuttgart, Stuttgart, Germany.
*Corresponding author. Email: frank.postberg@fu-berlin.de
†These authors contributed equally to this work.

diversity within salt-rich ice particles. Doing that, we identify different spectral subgroups within the group of Type 3 grains (see the "Basic spectral classification of Type 3 ice grains into Na- and K-rich groups," "Subclassifications of the Na-rich group," and "Subclassifications of the K-rich group" sections).

Impact speed—in addition to composition—is known to have a strong influence on the appearance of CDA cation mass spectra (*9*, *10*, *12*, *18*) because ions are created by impact ionization of an impinging ice grain. The CDA dataset was recorded at a wide variety of ice grain impact speeds at hypervelocities ranging from about 4 to 16 km/s. Therefore, we investigate the influence of impact speed on the spectra to disentangle it from the ice grain composition (see the "Impact speed dependence of subtype frequencies and their spectral appearance" section).

We find an astonishing compositional diversity within the ensemble of salt-rich grains (see the "Review of salt separation from CDA results shown in the previous sections" section). Using laboratory experiments to simulate the freezing process of water droplets of oceanic composition, we show how this diversity could originate from segregated salt precipitation during freezing and infer the physical and chemical conditions inside Enceladus' ice vents that could produce the observed compositional subtypes (see the "Analog experiments simulating the freezing of oceanic spray" section). In parallel, we simulate the freezing process by thermodynamic equilibrium calculations from a starting solution with the same composition used in the experiments (see the "Thermodynamic equilibrium calculations" section).

In Discussion, we first compare CDA data with our simulations (see the "Comparison of CDA data with freezing experiments and thermodynamic calculations" section) before discussing implications for the conditions inside Enceladus' ice vents for droplet formation, droplet freezing, and their subsequent disintegration (see the "Implications for the conditions inside Enceladus' ice vents" section). From that, we propose a previously unidentified formation process for ice grains in the plume (see the "Multicomponent plume formation process" section) and conclude by describing a general chemical separation of both inorganic and organic oceanic species into differently composed ice grains ejected into the plume with implications for future plume sampling (see the "Implications for ice grain properties ejected into the plume and the E ring" section).

A description of the CDA dataset and the methods used for its analysis are found in the "Cosmic Dust Analyzer" and "E ring CDA data analysis" sections, respectively. The methods used in the freezing experiments and the thermodynamic equilibrium calculations can be found in the "Freezing experiments" and "Thermodynamic equilibrium calculations" sections. The sections in the Supplementary Materials (sections S1 to S3) provide additional information on CDA data analysis (section S1), freezing experiments (section S2), and ice grain formation (section S3).

RESULTS

CDA analysis of compositional variation in the population of salt-rich ice grains

Basic spectral classification of Type 3 ice grains into Na- and K-rich groups

Using the definition for Type 3 in Methods (see the "Spectral analysis" section), 961 Type 3 spectra are identified in the E ring CDA dataset used for this work. We found that most Type 3 spectra show strong sodium features with little or no potassium, while a smaller fraction shows substantial potassium features. In addition to peaks of monatomic Na^+ and K^+ ions as discrimination criteria, salt cluster ions are used, which consist of at least a cation (K^+ or Na^+) and additional neutral salt molecules [such as Na^+(NaOH), Na^+(NaCl), K^+(KOH), and K^+(KCl)].

We divide Type 3 spectra into Na- and K-rich groups by the following criteria:

1) Na-rich spectra have a peak amplitude ratio of $Na^+/K^+ > 10$.

2) K-rich spectra have a peak amplitude ratio of $Na^+/K^+ < 10$.

In case the peak amplitude ratio of Na^+/K^+ cannot be determined because recording of the spectrum was triggered by Na^+ (and the peak is thus not part of the recorded mass range; see the "Cosmic Dust Analyzer" section), the presence or absence of Na- or K-containing salt clusters is used as an alternative discriminator:

3) If K clusters of the form K^+(KOH) [95 unified atomic mass units (u)] or K^+(KCl) (113 u) are present, it is categorized as K-rich.

Importantly, in previous work (*9*, *14*), K-rich spectra have mostly not been considered because, at that time, their spectral signature was generally not identified as salt-rich. In (*9*), only one spectrum belonged to the K-rich group (with both Na and K salts present) but was not identified as a different class.

Here, we identify 62 K-rich and 899 Na-rich Type 3 spectra. Of 899 Na-rich Type 3 spectra, 858 exhibit a number of regularly reoccurring features. That can be used for further subclassification (see the "Subclassifications of the Na-rich group" section) and the group is named regular Na-rich. The rest (41 of 899) of the Na-rich Type 3 spectra do not have regular spectral profiles, often caused by instrumental distortion effects. These spectra cannot currently be subclassified and are named irregular Na-rich spectra, henceforth called Type 3 Na_Irr.

Subclassifications of the Na-rich group

Within the regular Na-rich spectra, the presence of four different salts can be identified by respective cation cluster species

$$\text{Chloride} \rightarrow Na^+(NaCl)_{1,2,3}$$

$$\text{Carbonate} \rightarrow Na^+\left(Na_2CO_3\right)$$

$$\text{Phosphate} \rightarrow Na^+\left(Na_3PO_4\right) \text{ and } Na^+\left(Na_2HPO_4\right)$$

$$\text{Hydroxide} \rightarrow Na^+(NaOH)_{1,2,3,4}$$

The peak intensities always decline from lower to higher order [e.g., $Na^+(NaOH) > Na^+(NaOH)_2 > Na^+(NaOH)_3$]. While hydroxide features are ubiquitous in all spectra—with one notable exception—chloride and carbonate features rarely coexist in the same spectrum, and phosphate spectra always appear without any carbonate and chloride features. There is also a large group of spectra that show only a hydroxide cluster and neither chloride nor carbonate.

On the basis of the anions seen in the different spectral groups, we define the following Na-rich subtypes and show coadded spectra of each subtype. The exact spectral definitions of all Type 3 subtypes listed below are given in section S1.1 of the Supplementary Materials.

Type 3 Na_Cl: chloride-rich / carbonate, phosphate not detectable (Fig. 1A).

Type 3 Na_Car: carbonate-rich / chloride, phosphate not detectable (Fig. 1B).

Type 3 Na_Mix: both chloride and carbonate detectable (Fig. 1C).

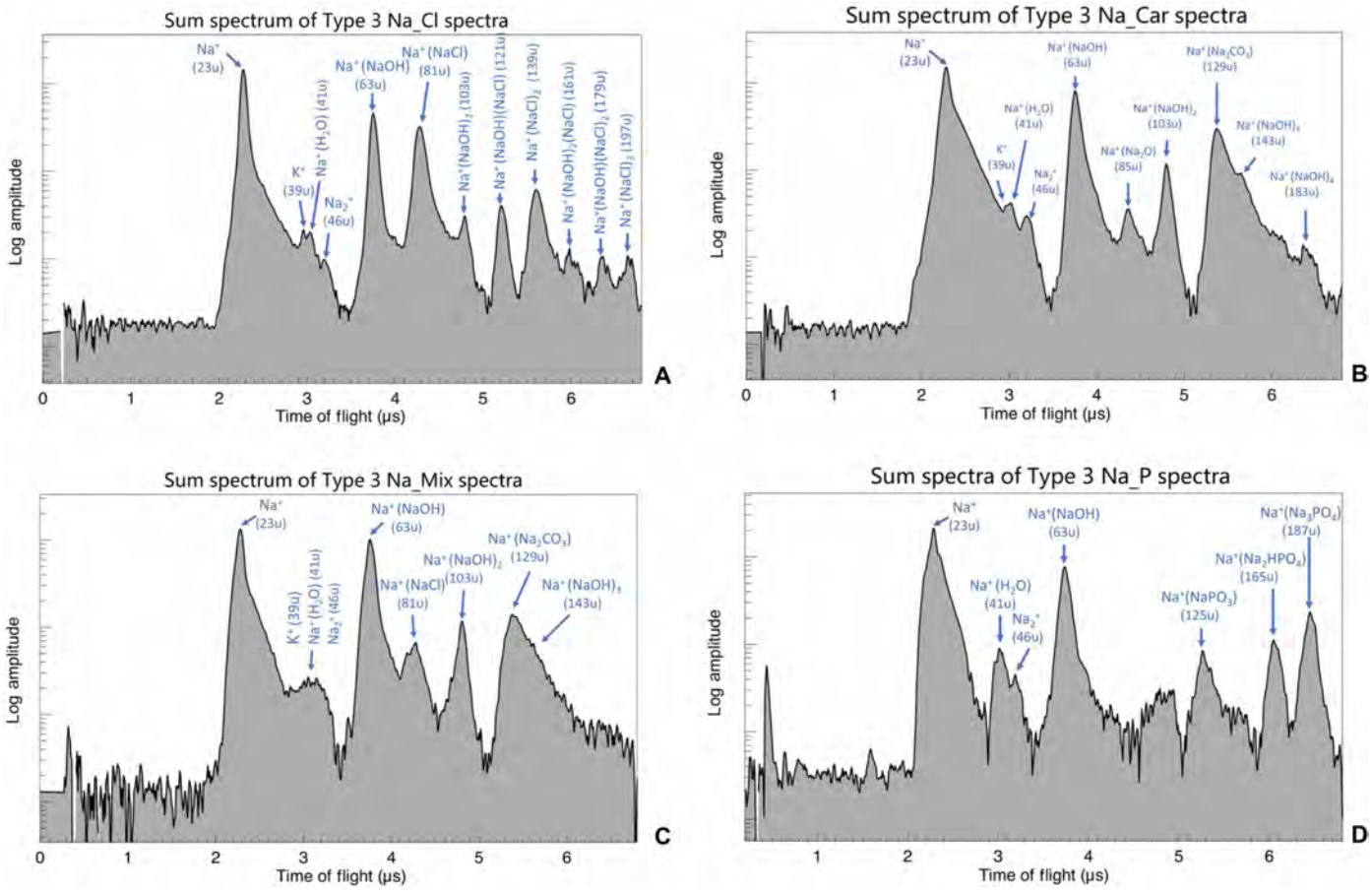


Fig. 1. Sodium rich E ring spectra showing chlorides, carbonates, and phosphates. Coadded E ring spectra of Type 3 Na_Cl (**A**), Type 3 Na_Car (**B**), Type 3 Na_Mix (**C**), and Type 3 Na_P (**D**). The number of spectra used is 148, 148, 10, and 9, respectively; a baseline correction has been applied. To limit effects resulting from the high impact speed of ice grains (see the "Impact speed dependence of subtype frequencies and their spectral appearance" section), only spectra from ice grains with an impact speed below 10 km/s were coadded, with the exception of Type 3 Na_P. Because of the small number of Type 3 Na_P spectra, we coadded all nine spectra of the original publication (*16*). To assure conformity, we only used spectra that have been triggered by the impact itself (see the "Cosmic Dust Analyzer" section). The labeled mass is that of the most abundant isotope. Note that both the defining ion of Type 3 Na_Cl [$Na^+(Na^{35}Cl) \rightarrow 81$ u] and a common water cluster of the hydroxide ion of the form $Na^+(NaOH)(H_2O)$ (81 u) share the same integer mass, and the latter species therefore could in principle lead to a false-positive detection of this subtype. In Methods (see the "Spectral analysis" section), we show how this problem was solved.

Type 3 Na_P: phosphate-rich / chloride, carbonate not detectable (Fig. 1D) (*16*).

Type 3 Na_OH: only hydroxides detectable (Fig. 2A).

Type 3 Na_U: assignment to one of the above subtypes uncertain (U) because of insufficient signal-to-noise ratio (SNR) (Fig. 2B).

Type 3 Na_U categorizes spectra that only show hydroxide peaks (as Type 3 Na_OH) but have a low SNR that often would not allow the identification of the smaller chloride or carbonate features, even if these compounds were present in the particle. As a discriminator between Type 3 Na_U and Type 3 Na_OH, we use the SNRs of $Na^+(NaOH) < 10$ for Type 3 Na_U and $Na^+(NaOH) > 10$ for Type 3 Na_OH.

In the coadded spectra shown here, we excluded those individual spectra that were recorded at impact speeds above ~10 km/s (method described in the "Identifying Type 3 spectra" section) because we find that spectral appearance and frequencies sometimes change at such high impact velocities (see the "Impact speed dependence of subtype frequencies and their spectral appearance" section).

For further classification of Type 3 Na_Cl, there is a single spectrum in the dataset with a sufficient SNR level not showing OH-related peaks of the form $Na^+(NaOH)_n$. Because the absence of hydroxides is outstanding from the rest of the dataset, we define another family of subtype Cl:

Type 3 Na_Cl_Cl: Type 3 Na_Cl spectra without hydroxide cations.

Type 3 Na_Cl_OH: hydroxide-bearing Type 3 Na_Cl spectra.

The only Type 3 Na_Cl_Cl spectrum is shown in Fig. 3A.

For further classification of Type 3 Na_Car, in addition to $Na^+(Na_2CO_3)$ (129 u), many Type 3 Car spectra show a smaller oxide peak at $Na^+(Na_2O)$ (85 u). Therefore, we define two families within the Type 3 Car subtype:

Type 3 Na_Car_O: Type 3 Na_Car spectra with $Na^+(Na_2O)$ (85 u). Here, the suffix O represents the oxide of Na.

Type 3 Na_Car_OH: Type 3 Na_Car spectra just with hydroxides but without an additional peak $Na^+(Na_2O)$ (85 u).

The coadded spectra of these two families—Na_Car_O and Na_Car_OH—are shown in Fig. 3B.

Subclassifications of the K-rich group

The K-rich group is separated from the Na-rich group by the presence of a significant K peak with an amplitude ratio $Na^+/K^+ < 10$ that always coincides with a change in spectral appearance by the

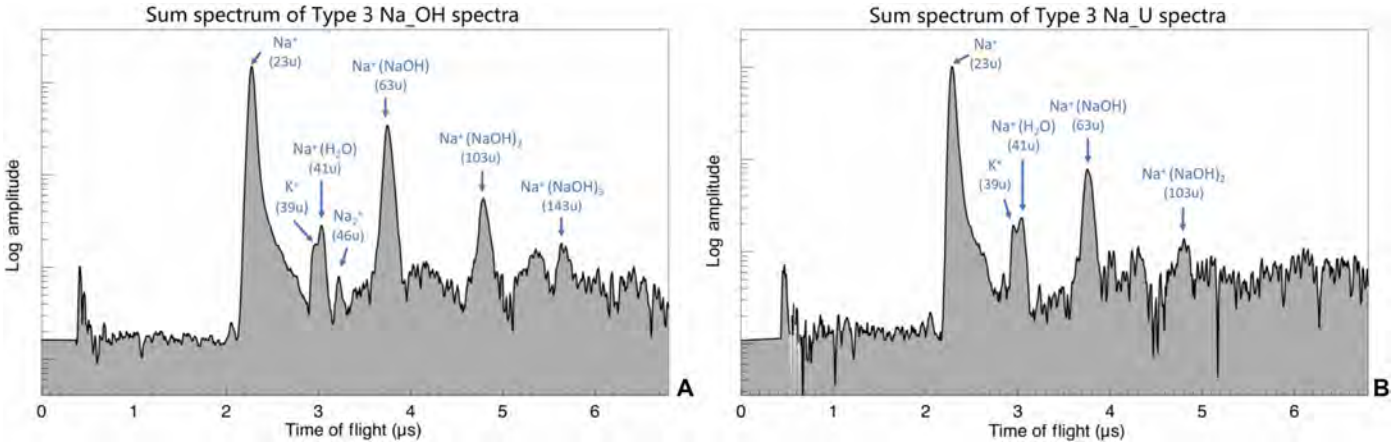


Fig. 2. Sodium rich E ring spectra showing only hydroxides. Coadded E ring spectra of Type 3 Na_OH (**A**) and Type 3 Na_U (**B**). The number of spectra used is 115 and 97, respectively; a baseline correction has been applied. To limit effects resulting from the high impact speed of ice grains (see the "Impact speed dependence of subtype frequencies and their spectral appearance" section), we only coadded spectra from ice grains with an impact speed below 10 km/s here. To assure conformity, we only used spectra that have been triggered by the impact itself (see the "Cosmic Dust Analyzer" section). The labeled mass is that of the most abundant isotope.

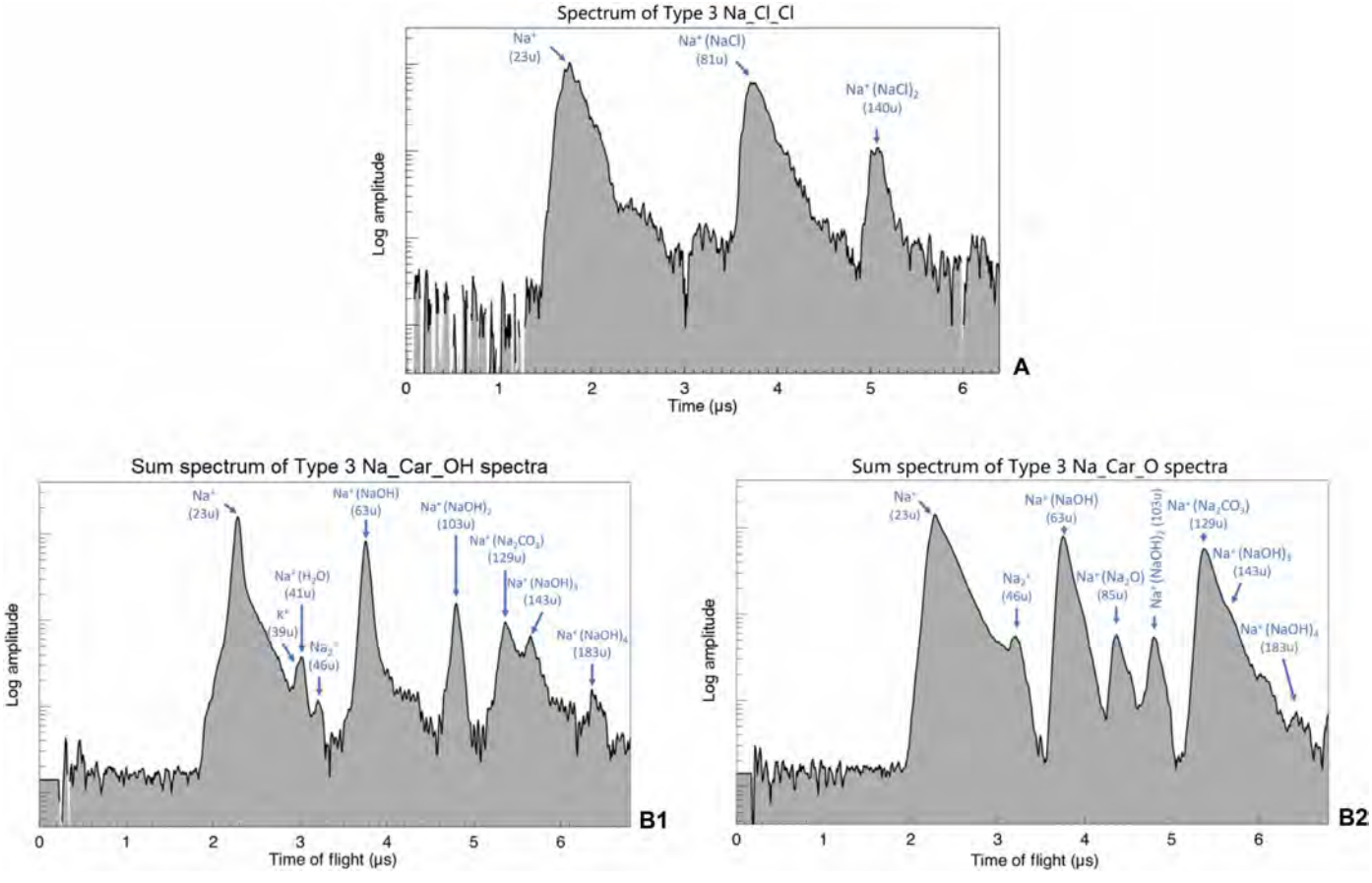


Fig. 3. Specific families of Type 3 Na_Cl and Type 3 Na_Car. (**A**) Only Type 3 Na_Cl_Cl spectrum in the dataset and the only Type 3 spectrum not showing any hydroxide features. (**B**) Coadded spectra of Type 3 Na_Car_OH and Type 3 Na_Car_O recorded at an impact speed up to 10 km/s.

addition of K-bearing salt cluster peaks. There are some systematic differences in the K-rich group compared to the Na-rich group:

1) All K-rich spectra are considered to be "regular" Type 3 spectra; there are no "irregular" ones as in the Na-rich group.

2) All spectra of this group show potassium chloride peaks of the form $K^+(KCl)_n$. In contrast to the Na-rich group, there are no phosphate or carbonate clusters (equivalent to Na-rich Type 3 Na_Car) and no spectra that exclusively show hydroxides (equivalent to Na-rich Type 3 Na_OH).

3) As in the Na-rich group, all K-rich spectra—in addition to chloride—show hydroxide features, here appearing as potassium hydroxide cluster ions of the form $K^+(KOH)_n$. Some spectra additionally show sodium hydroxides.

4) A few K-rich spectra have a peak consistent with $K^+(K_2O)$ [equivalent to $Na^+(Na_2O)$ in Type 3 Na_Car_O].

Depending on their Na/K ratio, K-rich spectra form two distinct subgroups. The exact spectral definitions of all Type 3 subtypes are given in section S1.1 of the Supplementary Materials.

Type 3 K_Cl: potassium-rich, sodium-poor spectra. These spectra always show a chloride feature (Fig. 4A).

Type 3 KNa: both potassium and sodium features in spectra (Fig. 4B). This spectral class shows a variety of spectral features reassembling all permutations of mixing Type 3 K_Cl with any of the Na-rich subtypes 3 Na_Cl, 3 Na_Car, or 3 Na_OH. In Type 3 KNa, mixed clusters with both sodium and potassium species in a single cation, e.g., $K^+(NaOH)$ or $K^+(NaCl)$, are frequent (Fig. 4B).

An overview of all subtypes in the dataset is given in Table 1 and Fig. 5.

Impact speed dependence of subtype frequencies and their spectral appearance

From the analysis of salt-poor E ring spectra of Type 1 and 2 (*10*–*13*), it is apparent that the impact speed has a nonnegligible influence on the appearance of CDA impact ionization spectra. In particular, water cluster formation largely depends on impact speed (*10*, *18*, *19*). Thus, impact speed can influence the peak's amplitude ratio and probably even the spectral subtypes produced by ice particles with the same composition. The speed dependence of Type 3 spectra has not been previously investigated but is important here because the dataset was recorded over a wide range of impact speeds, ranging from about 4 to about 16 km/s.

While the water cluster sequence $(H_2O)_nH^+$ forms the "backbone" in salt-poor spectra of Types 1 and 2, it is the sequence of $(NaOH)_nNa^+$ ($n = 1$ to 4 but typically just 1 and 2) in all Type 3 spectra of the Na-rich group. Although there is some indication of a decrease in amplitude of the $n = 2$ cluster in favor of the $n = 1$ species with increasing speed (tables S1 to S3), this is much less pronounced than for the water cluster sequence in salt-poor spectra.

However, a clear speed dependence can be observed for the defining features of Type 3 Na_Car $Na^+(Na_2CO_3)$ (129 u) and $Na^+(Na_2O)$ (85 u). Table S1 shows that both the amplitude ratios of $Na^+(Na_2CO_3)$ (129 u) and $Na^+(Na_2O)$ (85 u) to Na^+ (23 u) monotonically decrease with increasing impact speed. The decreasing fraction of Na_Car_O spectra above an impact speed of ≈6 km/s (fig. S2), which require the presence of $Na^+(Na_2O)$ (85 u) as the defining peak, is additional evidence for this speed dependence: The amplitude of $Na^+(Na_2O)$ (85 u) drops markedly (table S1), and with that, the occurrence of Na_Car_O spectra decreases (fig. S2) above ≈6 km/s, while the fraction of Na_Car_OH spectra increases (fig. S2).

The following relations illustrate schematically how the sodium oxide cation could be formed from a carbonate cation at low-speed impacts onto CDA, while at higher impact speeds, carbonate and oxide preferably disintegrate completely with the release of CO_2.

Low-speed case (relation A)

$$Na^+(Na_2CO_3) \rightarrow Na^+(Na_2O) + CO_2$$

High-speed case (relation B)

$$Na^+(Na_2CO_3) \rightarrow 3Na^+ + O^{2-} + CO_2$$

$$Na^+(Na_2O) \rightarrow 3Na^+ + O^{2-}$$

Note that CDA can only detect cation species, while neutral and anions remain "invisible" to CDA.

Another speed-dependent trend is the apparent "migration" from Type 3 Na_U to Type 3 Na_OH. Figure S2 shows that the percentage of subtype Na_U in all spectra decreases markedly from 36% to about 2% at the highest impact speeds, whereas subtype Na_OH

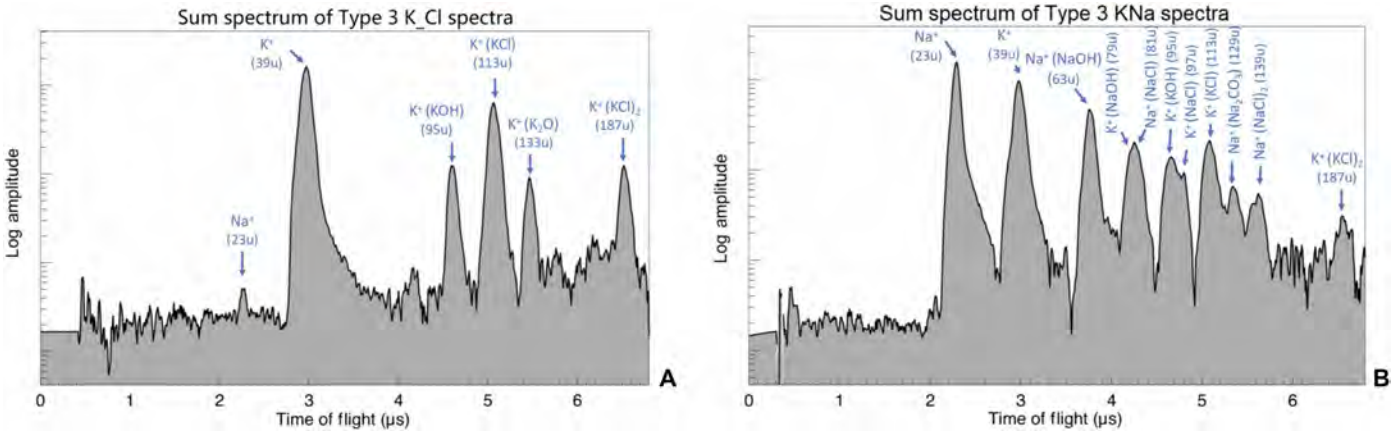


Fig. 4. Potassium rich E ring spectra. Coadded spectra of Type 3 K_Cl (**A**) and Type 3 KNa (**B**). Note that both of the most frequent Na cluster types $Na^+(NaCl)$ and $Na^+(Na_2CO_3)$ appear in (B). The total number of spectra used for coadding is 13 and 32, respectively. To assure conformity, we only used spectra that have been triggered by the impact itself (see the "Cosmic Dust Analyzer" section). The labeled mass is that of the most abundant isotope. Spectra were recorded at an impact speed below 10 km/s and are subject to a baseline correction.

Table 1. All new Type 3 subtypes identified in this work and their abundances. Two of the new subtypes are further categorized in two families. The main identified ion species are shown for each subtype. Note that the CDA can only detect cations, so the anions appear as part of a cationic cluster (also see definitions above and in section S1.1 of the Supplementary Materials).

Group	Subtype	Number	Families	Main cations	Main anions
Na-rich	3 Na_Car	224	129 Car_OH	Na^+	CO_3^{2-}, OH^-
			95 Car_O		CO_3^{2-}, O^{2-}, OH^-
	3 Na_Cl	222	221 Cl_OH	Na^+	Cl^-, OH^-
			1 Cl_Cl		Cl^-
	3 Na_Mix	12		Na^+	Cl^-, CO_3^{2-},OH^-
	3 Na_P	9		Na^+	PO_4^{3-}, HPO_4^{2-}, OH^-
	3 Na_OH	160		Na^+	OH^-
	3 Na_U	231		Na^+	OH^-, ?
	3 Na_Irr	41		Na^+	?
K-rich	3 K_Cl	20		K^+	OH^-, Cl^-, O^{2-}
	3 KNa	42		K^+, Na^+	OH^-, Cl^-, CO_3^{2-}

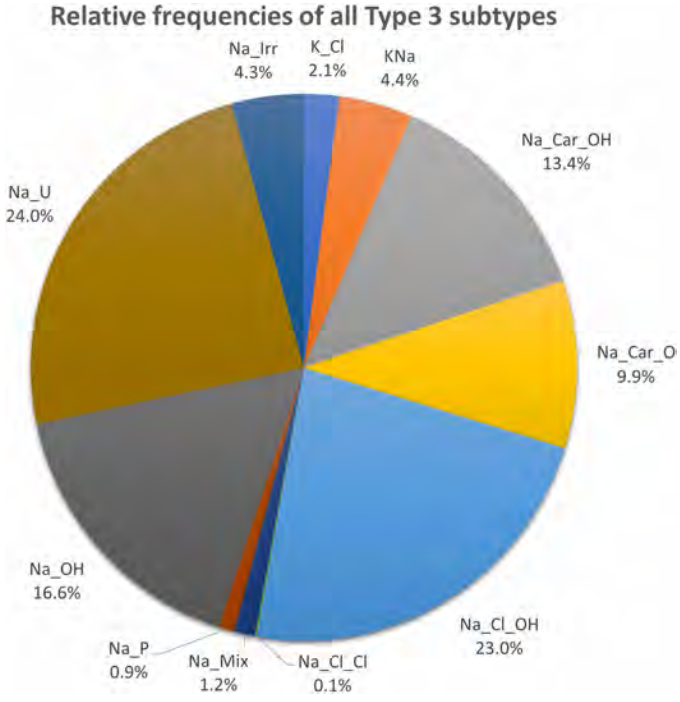


Fig. 5. Percentages of all Type 3 subtypes in the dataset.

increases from ≈15 to 44%. Note that the only difference between the spectral appearances of Type 3 Na_OH and Type 3 Na_U is the SNR of Na^+(NaOH) (63 u), and if faster impact speeds promote a stronger Na^+(NaOH) signal, subtype Na_U spectra might turn into subtype Na_OH or other subtypes (in case, e.g., chloride or carbonate features now appear because of the better SNR). Figure S3 shows how the SNR of Na^+(NaOH) (63 u) in Type 3 Na_OH increases significantly above impact speeds of 10 km/s. This indicates that subtype Na_U-to-Na_OH conversion is the main reason for the decreased proportion of Type 3 Na_U and increased proportion of Type 3 Na_OH above ≈10 km/s.

Notably, the defining ion in Type 3 Na_Cl, that is, Na^+(NaCl) (81/83 u), does not show any evidence for disintegration with increasing speed as $Na^+(Na_2CO_3)$ (129 u) and $Na^+(Na_2O)$ (85 u) in Type 3 Na_Car do. Table S2, illustrating the influence of speed on the characteristic peaks of Type 3 Na_Cl spectra, shows that by contrast, the amplitude of Na^+(NaCl) (81 u) only slightly increases with impact speed. This indicates a greater stability of the sodium chloride cation compared to the carbonate and oxide cations. The Na^+(NaOH) (63 u)–to–Na^+ (23 u) ratio likewise increases with speed in Type 3 Na_Cl (table S2).

Because the most substantial changes for both spectral appearance and frequency occur above ~10 km/s, we exclude these spectra from the coadded spectra representing the 'average" composition of each Type 3 subtype (Figs. 1 to 4). In section S1.3 of the Supplementary Materials, we discuss further details of the speed dependence on spectral occurrence in this dataset.

Review of salt separation from CDA results shown in the previous sections

From the comprehensive Type 3 dataset analyzed above, it is obvious that the different detected salt species do not often mix in a single E ring ice grain but appear separated in different grains, each time at strongly elevated concentrations compared to the salt-poor Types 1 and 2. The exception is that practically all spectra of the K- and Na-rich groups show the presence of hydroxides: NaOH features appear in all subtypes of the Na-rich group (Type 3 Na_Car, Type 3 Na_Cl, Type 3 Na_P, Type 3 Na_OH, Type 3 Na_Mix, and Type 3 Na_U), and KOH features appear in all spectra of the K-rich (Type 3 K_Cl) group and both Na and K hydroxide features together in the group rich in both Na and K salts (Type 3 NaK).

We investigated the statistical significance of this separation in section S1.4 of the Supplementary Materials. The statistically most significant example is that in Na-rich spectra, the presence of CO_3^{2-}-related peaks and Cl^--related peaks is mutually exclusive, with only 12 (1.4%) of 858 regular Na-rich CDA Type 3 spectra containing both carbonate- and chloride-related peaks (Type 3 Na_Mix in Table 1). These two chloride- and carbonate-rich subgroups show up in similar frequencies, and if their occurrence were statistically independent, one would expect about 88 mixed type spectra.

However, we find (Supplementary Materials, table S4) that the odds of finding chlorides are about 25 times lower if carbonate is present. Furthermore, applying the one-sided Fisher exact test (section S1.4 in the Supplementary Materials), we find $P < 10^{-10}$, demonstrating that the conclusion on CO_3^{2-}-related peaks and Cl^--related peaks being mutually exclusive is highly significant. The carbonate- and chloride-containing spectra are complemented by a much smaller population of sodium phosphate–rich spectra, which in turn never show any traces of chlorides or carbonates.

Similarly, Na and K salts are separated, albeit less strictly. Of a total of 961 Type 3 spectra, 42 show both salts in elevated abundances (section S1.4 in the Supplementary Materials). More specifically, this is 4.7% of all Na-containing spectra (899) but a substantial 68% of all K-rich spectra (*20*). Thus, >95% of all Na-rich spectra show almost pure Na salts, whereas only ≈32% of all K-rich spectra show almost pure K salts (Type 3 K_Cl). Note that, K-rich salts always are chlorides and never carbonates or phosphates but—like practically all Type 3 spectra—are always accompanied by hydroxides, in this case, K-hydroxides. Most K-rich spectra show a minor peak at 133 u, consistent with $K^+(K_2O)$. Some spectra of the Na-rich group (Type 3 Na_Car_O) likewise show a small oxide peak [$Na^+(Na_2O)$, 85 u]. However, while the Na-oxide feature exclusively appears in carbonate spectra, the K-oxide feature always coincides with chloride features.

There is a large group of Na-rich spectra—subtype Na_OH—showing just hydroxides but neither one of the other three anion types. Such a "hydroxide-only" population is missing in K-rich spectra, which always show both hydroxide and chloride features.

In conclusion, NaCl, Na_2CO_3, Na_3PO_4/Na_2HPO_4, and KCl appear mostly separated from grain to grain in the Type 3 population. The most notable exception is that high concentrations of KCl in many cases appear together with NaCl in roughly similar ion abundances but not vice versa. However, all subtypes come together with hydroxide, NaOH or KOH, respectively, in the same Type 3 ice grain (with the exception of only one Type 3 spectrum not showing hydroxides). There is also a relatively large fraction of Na-rich grains just showing NaOH without any other salts at detectable levels but no respective pure KOH population in the K-rich group.

When considering reasons for CDA's observation of salts showing up mostly separated in ice grains emitted by Enceladus, we regard it as highly unlikely that there are different water reservoirs of radically different composition feeding different parts of the plume. For example, both Na and K are conservative elements in aqueous geochemistry and should be mostly distributed into the liquid phase in water-rock reactions (*21*). Given that the Na abundance is greater than K in the solar abundance (*22*), K-rich and Na-depleted oceanic water cannot be formed in Enceladus through water-rock reactions and subsequent processes (e.g., degassing). Likewise, partial freezing of ocean water within fracture networks in Enceladus' icy crust before plume formation is unlikely to explain the observed segregation. Partial freezing can drive compositional changes in a fluid through salt precipitation, which affects the relative abundances of ions. It cannot, however, generate brines of wholesale different compositions in which specific ions have been almost entirely removed, as would be required to explain the Type 3 grain compositional subtypes. For instance, in computational simulations of freezing an Enceladus' ocean water simulant (*23*), the fluid at no point during freezing becomes dominated by carbonates or potassium, leaving the carbonate- and potassium-rich CDA subtypes unexplained. This means that even an elaborate series of fractures, where fluids experience different temperatures and, thus, different extents of partial freezing, cannot explain the distinct compositional subpopulations observed by the CDA.

We rather suggest that brine rejection in a freezing liquid of a rather homogeneous ocean composition—where each salt species crystallizes at a certain temperature—is responsible for the observed salt segregation.

Analog experiments simulating the freezing of oceanic spray

To constrain the mechanisms responsible for creating the compositional diversity of plume materials, we performed laboratory experiments simulating freezing of seawater droplets ascending in fractures of Enceladus' icy crust (see the "Freezing experiments" section for methods). The CDA ice grains analyzed in the "CDA analysis of compositional variation in the population of salt-rich ice grains" section have typical diameters on the order of 1 to 2 μm (*24*). In this section, we test the hypothesis that all observed salts stem from spray forming above a liquid reservoir of very similar composition (*9*, *13*, *14*) but become spatially separated inside these droplets by salt segregation induced by brine rejection during freezing. In contrast to previous assumptions [e.g., (*9*)], we hypothesize now that the droplet size of this spray can be much larger (10s or 100s of micrometers) than the sizes of ice grains observed in the plume (*24*, *25*) and that the formation of the much smaller salty plume grains occurs later, after the salt segregation but before emission into space. We will discuss a plausible mechanism for this fragmentation process in the "Fragmentation of large grains through wall collisions" section.

In the experiments, droplets of the Na-K-Cl-HCO_3-PO_4 solution (as an analog of Enceladus' seawater; see the "Freezing experiments" section and table S7) with different diameters (15, 200, and 1000 μm) were frozen at different cooling rates (from 1 K/min to >1000 K/min). Note that this diameter refers to the liquid state after the droplets had been put onto a plate and had notably flattened by gravity (aspect ratio of roughly 4:1), and the volume of a 200-μm-diameter droplet here would be roughly equivalent to a 120-μm-diameter spherical droplet. Then, the completely frozen droplets were freeze dried in a vacuum chamber, and the elemental compositions of the residual salt skeletons of the frozen droplets were analyzed using electron probe microanalysis (EPMA) with a horizontal spatial resolution of ~0.4 μm (see the "Freezing experiments" section for details). Because spatial resolution is comparable to the size of plume and E ring particles [e.g., (*6*, *14*, *22*)], our experiments can investigate the spatial distribution of individual salts in the frozen droplets on the scale of Type 3 ice grains that were analyzed by the CDA in the "CDA analysis of compositional variation in the population of salt-rich ice grains" section.

Typical top-down images of elemental mapping of freeze-dried droplets with a size of 200 μm at different cooling rates are shown in Fig. 6. This figure, supported by fig. S5, shows that micrometer-sized segregation of salts (i.e., separation of salt species on that scale) occurs within frozen droplets at relatively slow cooling rates (10 K/min or slower), whereas faster cooling (20 K/min or flash freezing) leads to a more uniform distribution (Fig. 6). These findings are consistent with previous experiments on slow and flash freezing of brine droplets (*23*).

This trend is quantified by histograms of the C/Cl ratio in Na-rich areas of droplets with sizes of 200 μm (Fig. 7) showing the degree of separation of Na chlorides from Na carbonates. At fast cooling (20 K/min and flash freezing), the log(C/Cl) value in Na-rich areas in the freeze-dried droplet exhibits a single peak at around zero, reflecting

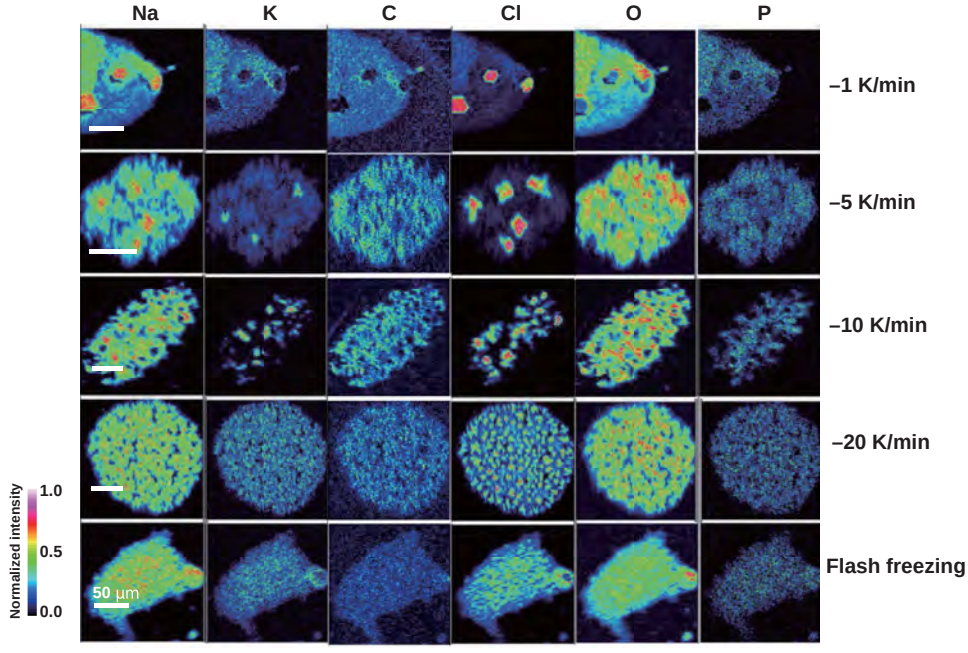


Fig. 6. Elemental mapping (top-down view) of freeze-dried droplets for different cooling rates. Details of the experimental setup can be found in the "Freezing experiments" section. Typical results for droplet sizes of ~200 µm are shown. Colors represent signal intensities of each element—shown at the top of each column—normalized by their highest intensities in the elemental map. Bars in each panel show the scale of 50 µm. With slower cooling rates, the size of chloride (Cl) salt patches—correlating with both Na and K—becomes larger, and their boundaries become more defined. Apparently, NaCl and KCl have precipitated inside the freezing droplets, whereas both Na carbonates and phosphates are present to fill the matrix. On the micrometer scale, however, C (the tracer for carbonates) and P (the tracer for phosphates) also appear at different locations in the droplets (fig. S5). When droplets were more rapidly cooled (20 K/min or flash freezing), all elements are ever more uniformly distributed.

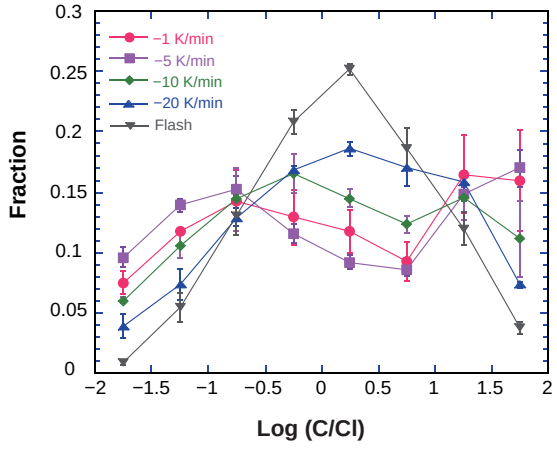


Fig. 7. C/Cl composition distribution in all Na-rich areas in freeze-dried droplets with the size of ~200 µm. Colors and symbols represent different cooling rates. The histogram bin size of the logarithmic *x* axis is 0.5. The Na-rich areas (Fig. 6) are defined as Na intensity >20% of the highest intensity in the elemental map (see the "Freezing experiments" section). Areas with K/Na > 0.05 were excluded to ensure a good representation of the two CDA Na-rich groups Type 3 Na_Cl and Type 3 Na_Car. The error bar at each point reflects the standard error obtained from the results of three freeze-dried droplets.

that the composition of the starting solution (C/Cl ~1) is also the most frequent case in the elemental maps. This indicates little segregation on the scale of Type 3 grains at these cooling rates. On the other hand, at a slower cooling rate (10 K/min or slower), the log (C/Cl) value of Na-rich areas shows two maxima with one peak at log (C/Cl) > ~1 (Na carbonates) and the other at log C/Cl < ~−1 (Na chlorides), signifying that one of the two salts dominates elemental mapping. Note that the segregation does not increase further when lowering the rate from −5 to −1 K/min.

We also find that in smaller droplets of 15 µm, the evolution of two separated maxima becomes less clear (consistent with the visual observations in elemental mapping; figs. S6 and S7). Inside such small droplets, even at the slowest applied cooling rate (−1 K/min), elements appear throughout the droplets without strong segregation.

An important constraint from CDA data is that the K-rich type exclusively appears in the form of chlorides (only mixed with the ubiquitous hydroxides), in stark contrast to the diversity of Na-rich subtypes. In Fig. 6, we show that for droplet sizes of 200 µm and cooling rates of 5 and 10 K/min, K is almost exclusively distributed in Cl-rich areas. However, this completely changes at the lowest rate of 1 K/min, where K appears to mostly coincide with carbonate (C-rich) spots (Fig. 6). Figure 8 shows the fractions of K-rich spots found in Cl-rich areas compared to all K-rich areas for different cooling rates and droplet sizes, i.e., corresponding to a fraction of KCl for all K-bearing minerals. For 1-mm-sized droplets, the chloride fraction starts to decrease significantly already at 10 K/min (Fig. 8). In contrast, for 15-µm droplets, the fraction of K in Cl-rich areas remains relatively high even at cooling rates of 1 K/min, but this is caused by the lower degree of segregation between K and Na chlorides in such small droplets (fig. S7). In summary, this suggests that precipitation of K carbonates, such as $K_2CO_3 \cdot 1.5H_2O$ and $KHCO_3$, may be inhibited by sufficiently fast cooling, the rate of which varies with the droplet size (>1 K/min for 200 µm and >10 K/min for 1000 µm). This observation thus limits the cooling rate at the low end, opposing the better segregation at cooling rates below 20 K/min.

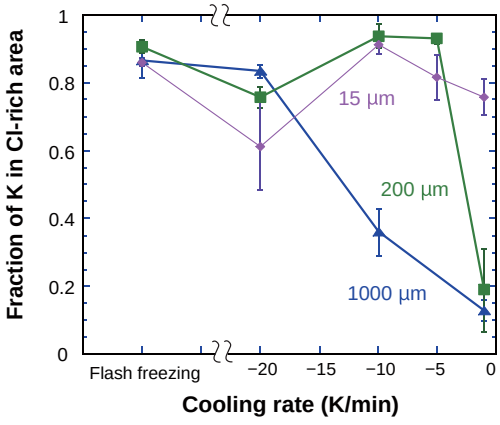


Fig. 8. Fraction of K in Cl-rich areas as a function of cooling rate. Colors and symbols represent different droplet sizes. The K-rich areas are defined as a pixel with K intensity >40% of the highest intensity in the elemental map (see the "Freezing experiments" section). Cl-rich areas are those pixels with >20% of the highest Cl intensity. The error bar at each point reflects the standard error obtained from three to six freeze-dried droplets.

Our freezing experiments indicate separation of NaCl and KCl at relatively slow freezing rates (Fig. 6). To quantify this separation, we compare log(Na/K) in Cl-rich areas for 200-µm-sized droplets for cooling rates of 5 and 20 K/min (Fig. 9). At 20 K/min, Na/K accumulates around log(Na/K) ~ 1.5, close to the initial Na/K ratio [log(Na/K) ~ 1.2] in the starting solution. Regions with log(Na/K) < −0.5, i.e., are practically absent at 20 K/min for the spatial resolution (~0.4 µm) of our analysis. With a slower cooling of 5 K/min, however, the ratio more clearly develops two maxima peaking at log(Na/K) ~2.0 (NaCl) and −0.5 [(Na,K)Cl]. At 5 K/min, there is a small but significant fraction with log(Na/Cl) ≤ −1.0 (KCl), which can be visually confirmed in the elemental map of Fig. 6. The Cl-rich areas with log(Na/K) > 1.0, −1.0 to 1.0, and <−1.0 at 5 K/min (Fig. 9) would correspond to the Type 3 Na_Cl, Type 3 KNa, and Type 3 K_Cl, respectively, identified by the CDA (Table 1).

At relatively slow freezing (e.g., 10 and 5 K/min), there are also Na-rich areas with very low Cl and C but high O, suggesting Na hydroxides to be the dominant salt there (Fig. 6; also see fig. S8 in details). Given that our thermodynamic calculations (see the "Thermodynamic equilibrium calculations" section) do not show precipitation of hydroxides under equilibrium conditions, we suggest that Na hydroxide could precipitate because of nonequilibrium CO_2 degassing. The O-rich areas (as a tracer for hydroxides) in Na-rich areas tend to appear around empty voids in elemental mapping (fig. S8). We interpret these voids as the remains of degassed CO_2 inside the freeze-dried droplets, and these correlate with locations of notable NaOH concentrations. In contrast to slow freezing, Na hydroxides seem to be absent in flash freezing (fig. S9). This may be because flash freezing would kinetically inhibit the nucleation and degassing of CO_2 bubbles.

In conclusion, our freezing experiments indicate an optimal segregation within a single droplet with a slow cooling rate (<≈20 K/min) in a relatively large droplet (>≈15 µm). However, to avoid the efficient formation of K carbonates, droplets should not cool too slow (>≈1 K/min).

Experimental limitations

The focus of the experimental design (see the "Freezing experiments" section) was to have optimal control over the freezing rate and droplet size and the ability to monitor all relevant salt species. That brought a few obvious differences to the freezing process of droplets in an Enceladus ice vent: The droplets in the experiments froze on top of a metal plate, subject to Earth's gravity, and they were exposed to ambient air while freezing. Because of the first point, droplets were substantially flattened (with an aspect ratio of about of 4:1) and started freezing from the bottom before the freezing of the entire surface by cooling of the ambient air began somewhat later. By contrast, on Enceladus, close-to-spherical droplets are free-floating and likely freeze symmetrically from the outside inward (see the "Timescales and condition for freezing of large droplets" section).

It is important to understand that the segregation of chlorides, carbonates, phosphates, and sodium and potassium shown in the figures of this section and the respective Supplementary Materials is "top-down views," only showing the segregation in the two horizontal dimensions and integrated over a greater part of droplet depth. However, in contrast to pure bottom-up freezing (*26*), salt species are also expected to segregate vertically within the droplet while freezing inward from its surface. We investigated this by performing elemental analysis at increasing electron accelerating voltages, probing the integrated elemental composition down to ever greater depth of the freeze-dried droplet. The elemental composition of the salt skeleton contains more Na carbonate closer to the surface, whereas those at greater depth contain more Na chloride (fig. S10). When freezing inward from the outside, Na chloride tends to be present in deeper parts of droplets because it should mostly precipitate at the last stage of freezing (see the "Thermodynamic equilibrium calculations" section) when a highly concentrated Na-K-Cl brine lastly solidifies close to the center of the droplet. Therefore, the degree of segregation inferred from the two-dimensional EPMA shown in this work constitutes a lower limit of the real three-dimensional segregation in the frozen droplet. This vertical segregation will be even more pronounced in a near-spherical droplet on Enceladus that froze more symmetrically from the outside inward compared to the flattened droplet resting on a plate that started freezing from the bottom in our experiment.

To investigate the effect of asymmetric freezing from below of a droplet resting on a metal plate in our experiments, we additionally conducted one experiment with droplets lying on a thermally better insulated glass plate. The disadvantage of this approach is that alkali metals and carbon could not be mapped with high accuracy (see methods in the "Freezing experiments" section). However, the segregation of chlorides and phosphates could be assessed. The results shown in fig. S11 indicate a much better separation of these two phases with a glass plate where the droplet has frozen more symmetrically from the outside inward (as it would on Enceladus) compared to the metal plate used in all other experiments of this work (with increased freezing from below). Even minor species, like phosphates, then separate well from the abundant chlorides.

Moreover, the spatial resolution of the analytical tools in our experiments (EPMA pixel size ≈ 0.4 µm) is a little larger than the expected salt deposits of typical Type 3 grains. For example, in an ice grain of 1 to 2 µm in diameter (the most frequent grain size in the CDA dataset), a salt deposit of 0.5 wt % salt would be only ≈0.1 to 0.2 µm in diameter. Therefore, pixels that appear unsegregated in

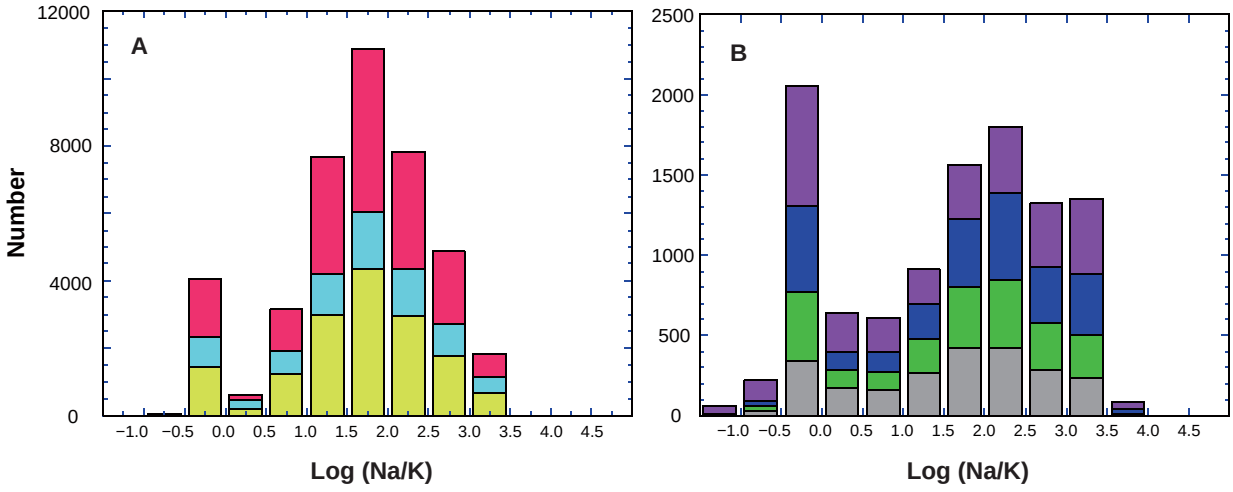


Fig. 9. Histograms of log(Na/K) composition in Cl-rich areas of freeze-dried droplets with a diameter of ~200 μm. Cooling rates at (**A**) −20 K/min and (**B**) −5 K/min. Cl-rich areas are defined as those pixels with Cl intensity >40% of the highest intensity in the elemental map (see the "Freezing experiments" section). In (A), three different droplets and, in (B), four droplets were analyzed for each cooling rate. The different colors in each histogram reflect the data from each droplet. The two maxima representing Na- and K-rich areas become more pronounced with slower cooling in each of these droplets.

the EPMA at this analytical resolution could plausibly still contain segregated salts at the relevant scale of Type 3 ice grains, and the degree of segregation we observe is therefore a lower limit.

In summary, the fact that we observe the segregation in only two dimensions viewing top-down onto a flattened droplet that has not frozen symmetrically on the one hand and the limitation in spatial resolution of elemental mapping on the other hand are limiting our assessment of salt segregation. The "real" segregation inside a droplet of similar size freezing inside an Enceladean ice vent at a similar rate should be better than the results shown in this work. Improved experiments are already in progress.

Thermodynamic equilibrium calculations

To further constrain the segregation of salts that is found in our experiments, we modeled equilibrium salt assemblages that form upon freezing of droplets with a composition used in the freezing experiments (see the "Freezing experiments" section and table S7) using the thermodynamic aqueous chemistry package PHREEQC (*27*). Slow cooling systems resemble equilibrium conditions better than fast cooling systems because the system has more time to reach a free energy minimum, meaning that there are less kinetic effects, such as supercooling (*19*).

In our models (Fig. 10), as the fluid starts to freeze at around −1°C, Na hydrogenphosphates first precipitate in a hydrated form (Na_2HPO_4:$12H_2O$). Then, Na carbonates follow, starting at around −4°C (natron, Na_2CO_3:$10H_2O$) and −20°C (nahcolite, $NaHCO_3$). Last, Na and K chlorides precipitate as hydrohalite (NaCl:$2H_2O$) and KCl between −22.5° and −24°C. About 90% of the water ice freezes between −1° and −5°C. In a second step between −23° and −24°C, practically all of the remaining liquid freezes, coinciding with chloride precipitation (Fig. 10).

Note that the sequence of carbonate precipitation is very sensitive to the pH that is determined here by the carbonate/chloride ratio of the starting solution. For example, refs. (*19*) and (*23*) used a lower carbonate/chloride ratio with the result that both carbonate species had precipitated at much higher temperatures. Depending on this ratio, either carbonate or bicarbonate generally starts to precipitate between −4° and −8°C, and bicarbonate/carbonate speciation then solely depends on the pH of the remaining solution: If pH is above pH ≈ 9.8, carbonate precipitation dominates, whereas below pH ≈ 9.6, bicarbonate precipitation dominates.

The pH value of the remaining liquid solution changes throughout the freezing process (Fig. 10). When the liquid solution cools and the first H_2O crystallizes, pH slightly increases up to a maximum of 11 and then remains almost unchanged by the precipitation of hydrogenphosphates. As soon as carbonates begin to precipitate, the pH goes down, reaching a minimum of about 9.8 shortly before bicarbonate precipitation starts and only slightly changing upon chloride precipitation and then going up again until the simulation stops.

To allow for efficient spatial segregation, salt precipitation events should be separated in time during the freezing of a droplet. Given that freezing progresses over time, the relative timings of salt precipitation events are given by their precipitation temperatures. Salts that precipitate mostly at similar temperatures would have less time to become spatially separated than those that precipitate mostly at very different temperatures. The quantity of each salt produced as a function of temperature (for an ideal equilibrium case) is shown in the second panel of Fig. 10. Note that this calculation represents indefinitely slow cooling, and therefore, kinetic effects are not considered. Still, this can be expected to be a good approximation of the relatively slow cooling used in the freezing experiments. In reality, salt precipitation kinetics may play a role in defining the mineralogical composition of ice grains, particularly if the kinetics of nucleation or growth differ substantially between different salt phases that precipitate. This should be an area for future study. Nevertheless, different nucleation or growth kinetics among the salts may increase the tendency for spatial segregation by separating the precipitation of specific phases by wider ranges of temperature (for instance, if a phase supersaturates before beginning to precipitate).

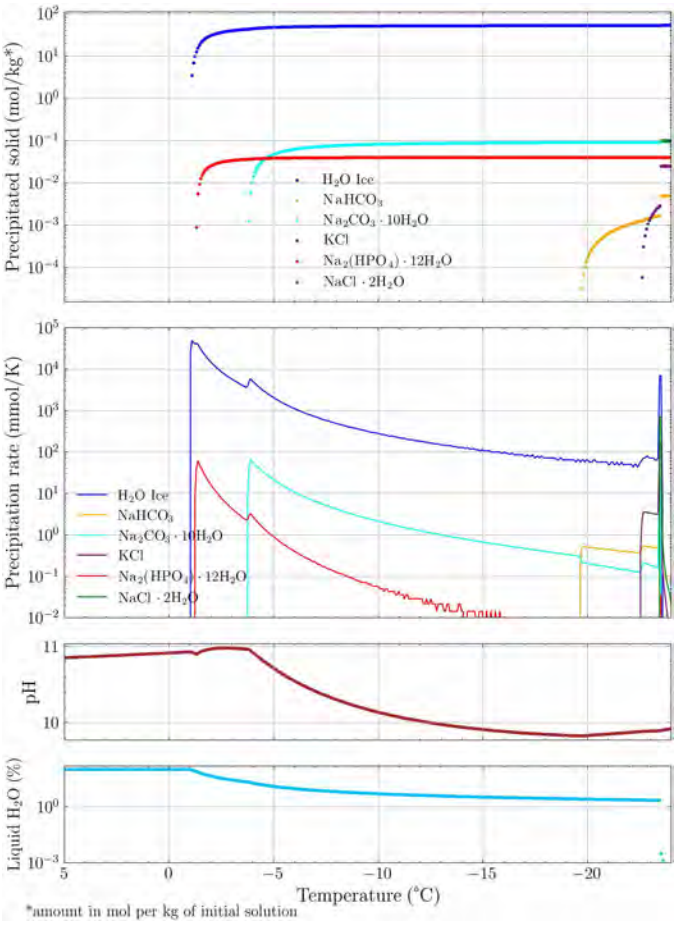


Fig. 10. PHREEQC chemical equilibrium calculations simulating the freezing of the solution used for the freezing experiments with decreasing temperature. The top panel shows the total precipitation of different salts, the middle panel shows the precipitation rate, and the two bottom panels show the evolution of the pH and the fraction of remaining liquid compared to the starting volume.

Salt precipitation starts with Na hydrogenphosphate formation occurring in isolation, in good agreement with CDA observation that phosphates (Type 3 Na_P) are never observed mixed with chloride or carbonate. Note that the hydrated forms predicted in some cases by the equilibrium calculations (e.g., Na_2HPO_4:$12H_2O$) are indistinguishable from their pure forms (e.g., Na_2HPO_4) in CDA ice grain spectra. The rate of carbonate precipitation (in terms of moles precipitated per kelvin of cooling) starts at about two orders of magnitude above hydrogenphosphate, which continues to precipitate at much lower levels. Such low phosphate levels would probably go undetected in carbonate-rich CDA spectra, in good agreement with the large carbonate-rich population (Type 3 Na_Car). With the mixing ratios used in our freezing experiments, bicarbonate precipitation starts when the solution pH goes down to 9.8. The precipitation rate of bicarbonate is only slightly higher than the still ongoing carbonate precipitation. Given that carbonates and bicarbonates can currently not be distinguished by the CDA, this change would go undetected in CDA spectra. Last, chloride precipitation takes over at about −22.5°C. First, only KCl precipitates—well represented by Type 3 K_Cl in CDA data—and shortly after, when NaCl completely precipitates, the latter clearly dominates the mass of precipitated salts until −24°C. The remaining KCl precipitates together with similar amounts of NaCl, in good agreement with CDA's Type 3 KNa population showing both species.

Na hydroxide does not appear in the thermodynamic equilibrium calculation, because pH values remain too low (*28*). As we have seen in the previous section, hydroxide formation may be triggered by localized nonequilibrium outgassing of CO_2 gas in the droplet. We will discuss this process further in the following sections.

DISCUSSION

Comparison of CDA data with freezing experiments and thermodynamic calculations

The simplest explanation for the existence of compositionally distinct subpopulations of Type 3 grains is that the grains encountered by the CDA were fragments of initially larger parent grains, in which solid salts were physically segregated before fragmentation (see the "Implications for the conditions inside Enceladus' ice vents" section). Accordingly, the composition of each subtype observed in CDA data is inherited from the composition of regions within the parent grains. Taking this view, most aspects of the CDA observation are in qualitative agreement with the freezing experiments and the thermodynamic calculations, such as follows:

1) Clear separation of chlorides, carbonates, and phosphates: The physical separation of chlorides, carbonates, and phosphates in most cases can be satisfactorily explained by their precipitation being separated in time during droplet freezing. Given that different salts precipitate at different temperatures, slow cooling rates ensure that salt precipitation events are well separated in time, allowing for precipitated salts to become spatially separated from residual brine, within which the next salt species precipitates, and so on [e.g., (*23*)]. Thermodynamic modeling indicates that chlorides, phosphates, and carbonates should precipitate in different temperature ranges, and our experiments indicate that when the freezing is slow enough (<−20 K/min), their spatial separation is usually larger than the typical grain size of Type 3 ice grains. The rare coexistence of both chlorides and carbonates on the submicrometer scale is also in good agreement with CDA results and supported by thermodynamic modeling. Although thermodynamic modeling suggests that both carbonates and bicarbonates form, these are neither distinguishable by the CDA nor the analytical methods used in our freezing experiments.

2) Less clear separation of K salts from Na salts: Although more than 97% of Na-rich grains detected by the CDA (all Types except Type 3 K_Cl) show no or very low levels of K, only about 32% of K-rich grains (Type 3 K_Cl and Type 3 NaK combined) show no or very low levels of Na, while the rest show high levels of both K and Na (Table 1). This agrees well with both the experiments and thermodynamic calculations, wherein Cl-rich areas are more commonly found with high Na, with a smaller proportion of areas in which K and Na are at similar abundances (Fig. 9). Such a less pronounced separation of K and Na chlorides can be explained by thermodynamic calculations, in which most of the KCl precipitates at similar temperatures as $NaCl{\cdot}2H_2O$ (Fig. 10).

3) Potassium only forms chlorides: While Na appears in four different CDA spectral subtypes, each time with a different anion (chlorides, carbonates, phosphates, and even hydroxides), K only forms a chloride subtype. This is in good agreement with the experiments if

the freezing rate is faster than −1 K/min. At yet slower rates, K associates with C, suggesting the formation of K carbonates, which do not appear in CDA data. Thermodynamic calculations also agree with K appearing exclusively as KCl within the limits of the modeled ion concentrations and phases available in the used database (*19*).

4) Hydroxide formation: In CDA Type 3 spectra, hydroxide peaks are ubiquitous and almost always appear in all subtypes together with carbonates, phosphates, and chlorides. While Na carbonates (*9*) and phosphates (*16*) resulting from their alkaline pH naturally form abundant hydroxides during the impact ionization process in the CDA when mixed with water, hydroxides only form a minor peak at best in spectra from NaCl solutions [e.g., (*29*)] because of their slightly acidic pH value. Notably, neither NaOH nor KOH forms in our thermodynamic equilibrium calculations at any stage. However, from the freezing experiments, we have an indication that local disequilibrium degassing of CO_2 from the freezing brine might form hydroxides (fig. S8). One possible explanation that should be investigated further is that if CO_2 degassing is most efficient immediately before complete freezing of the droplets, dissolved $\sum CO_2$ would then degas as the water activity approaches zero, possibly leading to alkalization and Na hydroxide precipitation in the remaining liquid. Given that this last major freezing step occurs between −23° and −24°C from a brine dominated by Na, K, and Cl (Fig. 10), hydroxide and chloride precipitation would coincide (Fig. 10). This could explain why in all but a single case, chlorides appear together with hydroxides of the dominating cation—either Na, K, or both— in CDA grains of Type 3 Na_Cl, Type 3K_Cl, and Type 3 NaK, respectively. Furthermore, if degassing is occurring in the final stages before complete solidification, the production of OH^- could remain highly localized to the degassing bubble and not dilute through mixing with the bulk droplet, preserving an enriched OH^- concentration in the final Na-K-Cl–dominated brine. Such an effect is not captured by the thermodynamic simulations, which assume perfect mixing of components at all stages. In addition, more than 20% of all regular Type 3 spectra are ice grains that only show NaOH without any other salt species (Type 3 Na_OH; Fig. 2A). This might reflect the fact that even salt species precipitating at the same temperature and time in a droplet can still be spatially segregated [e.g., (*30*)]. However, the absence of a KOH subtype is currently very poorly understood. While KOH is clearly apparent in all KCl-rich ice grains, it does not form a subtype of its own with just KOH, as it is observed for NaOH in Type 3 Na_OH.

There are some other minor aspects in the CDA dataset, notably the degree of segregation of sodium species and the high levels of K in the K-rich group, that are currently poorly reproduced by our experiments (see the "Experimental limitations" section) and thermodynamical modeling. We explore this in more detail in the Supplementary Materials (section S2.1 there). Nevertheless, experimental and theoretical findings demonstrate the ability of freezing-driven salt precipitation to produce, under certain conditions, segregation qualitatively similar to the CDA data. In the following sections, we explore the implications of these findings for the understanding of the plume formation process at Enceladus.

Implications for the conditions inside Enceladus' ice vents

Our findings set previously unknown constraints upon the conditions and physical processes operating within the plume source vents at Enceladus. In order for fragmentation of larger grains to produce the subtypes observed by the CDA, our experiments and simulations require that (i) freezing must occur within relatively large droplets (~20– to 1000 μm), (ii) freezing of parent grains progresses relatively slowly (<20 K/min) to produce sufficient segregation, and (iii) larger parent droplets must have frozen sufficiently to precipitate salts before fragmentation, because salt segregation is a consequence of the freezing process. In addition, the occurrence of very few mixed types in CDA data requires that parent grains are efficiently fragmented.

Formation of large droplets by bubble bursting

Type 3 grains have been suggested to originate as salty drops of water from the Enceladean subsurface ocean dispersed by the bursting of bubbles of ascending gases (*9*, *14*). Bubble bursting should occur within icy vents hundreds of meters beneath the surface (see section S3.1 in the Supplementary Materials). Organic matter, forming an enriched layer at the water surface, may supply further materials to the droplets (*11*, *13*). Thermal convection as well as tidal driving of the subsurface plumbing system (*31*) and volatile exsolution (*32*) may lead to mixing of the water, driving turbulence and providing another mechanism for bubble formation.

Our experiments indicate that parent droplets much larger than the Type 3 grains are required to produce sufficient segregation to explain the CDA observations. There is a good reason to expect that droplets produced by bubble bursting at Enceladus should be sufficiently large. Droplet formation by bubble bursting is well studied for Earth's oceans [e.g., (*33*) and references therein] and recognized as an important process for delivering aerosols to the atmosphere. Laboratory studies of bubble bursting in terrestrial seawater have shown that droplet sizes are strongly dependent on bubble diameter, with larger bubbles of millimeters in size and above producing droplets 10s to 100s of micrometers in diameter (*34*), while smaller bubbles with diameters below 1 mm can produce submicrometer droplets (*35*). Recent calculations of hydrodynamic and hydrostatic scaling relations conducted in (*36*) show that rising bubbles and droplets produced by bubble bursting at Enceladus should be larger than those produced by similar processes on Earth. This is due mainly to much lower gravity in the Enceladus case. The typical sizes of droplets inferred in (*36*) produced by gas and water vapor bubbles are in the submillimeter range, which agrees with the droplet sizes required for segregation in the freezing experiments reported in the "Analog experiments simulating the freezing of oceanic spray" section. In addition, because our experimental droplets were not spherical, their effective volume is smaller than for an approximately spherical droplet with the same diameter (see the "Experimental limitations" and "Freezing experiments" sections). This means that parent droplets at Enceladus could be about 40% smaller than the droplet diameters investigated here and still produce the required segregation.

Timescales and condition for freezing of large droplets

Our experimental results (see the "Analog experiments simulating the freezing of oceanic spray" section) show that only cooling rates in the order of 10 K/min produced the observed degree of segregation (Figs. 6 and 7). This is in agreement with previous flash-freezing experiments, with cooling rates at about $\sim 10^3$ K min^{-1}, where the degree of segregation was likewise insufficient (*19*, *23*) to account for CDA observations. At these faster rates, a vitreous glass likely forms within the ice grains, which can crystallize if warmed, but leads to unsegregated salts (*23*). The observation of segregated salts in Enceladean ice grains is therefore an indication that freezing timescales must be slow enough to avoid such glass formation.

In the following, we will investigate whether conditions in the vents are in agreement with such slow cooling rates. We base all these considerations to the assumption of a quasisteady state such that the overall conditions in the vents have relaxed to a state that is close to thermodynamic equilibrium. Here, quasisteady means that the underlying variations of the plumbing system and the south polar terrain (like diurnal tidal stresses and changes in vent geometry by gradual ice sublimation on the vent walls) are slow compared to the processes of grain transport and the associated thermal adaption to the vertically changing conditions in the vents (more details in the Supplementary Materials, section S3.1). In the gas directly above the water, ≈100-μm-sized droplets are present as spray resulting from bursting bubbles of volatile gases ascending from the water column below. For plausible gas velocities in the vents (above centimeters per second) and gas densities (above 10% of the triple point density), droplets of this size are easily supported by friction in the ascending gas flow (fig. S13).

The gas should be locally in thermal equilibrium with the ice walls (section S3.1 in the Supplementary Materials). When the vapor, with the entrained water droplets, gets accelerated in the vents, ultimately streaming to the moon's surface, the pressure must drop and the temperature must decrease. In the steady flow of gas to the surface, the vapor becomes supersaturated (*37*, *38*), a situation that thermodynamically favors condensation and homogeneous nucleation of ice. The question arises where and under which conditions the droplets freeze and break up to fragments of the much smaller size range observed by the CDA.

For freezing, in principle, two cooling processes come into question during the transport of the droplets to the surface. These are, on the one hand, the radiative interaction with the vent walls and, on the other hand, the exchange of heat with the ambient gas and the droplet surface by evaporation of (mainly) water gas. To estimate the cooling rates associated with radiation, we followed the approach in (*39*) using more recent optical constants for water published in (*40*). For a rough estimate of the cooling of ice droplets by sublimation, we followed the approach in (*41*) using the Hertz-Knudsen law. We examine radiative and evaporative cooling for the case of a droplet of 200 μm in diameter at a temperature of 270 K situated between two ice walls that have a temperature of 269 K (fig. S12). Between the ice walls, there is water vapor at thermal equilibrium with these walls. While radiative loss leads to a temperature drop of about 1 K in about 1 min (reaching the 269 K of the ambient vapor), evaporative cooling does this in a fraction of a second. At the final temperature, the droplet diameter has reduced by evaporative loss by only little more than 0.1 μm (fig. S12). Repeating the calculation for various wall temperatures and droplet sizes shows that the evolution toward equilibrium is always driven by evaporation.

Droplets will therefore always rapidly equilibrate to the local wall temperatures. Thus, to achieve slow cooling rates in agreement with CDA measurements (see the "CDA analysis of compositional variation in the population of salt-rich ice grains" and "Analog experiments simulating the freezing of oceanic spray" sections), they must not be exposed to wall temperatures that are much cooler by, e.g., 10s of kelvins. We instead propose a situation where the ice below the south polar terrain and the whole plumbing system is thermally in a steady state. In particular, in the upper parts of the vents, the deposition of latent heat on the icy vent walls by condensing vapor is nearly balanced by radiative loss at the surface (*38*). For the ice walls in the vents, this implies gradually decreasing temperatures from the water table (close to triple-point conditions) up to the surface at a much colder temperature of not more than about 195 K (*42*). The gas rising in the vents locally adapts to the equilibrium pressure that corresponds to the temperature of the ice (*38*).

A droplet dispersed by bubble bursting will initially be at the temperature of the ocean water. The gas, however, will experience a slight temperature drop that arises from the conversion of internal heat to kinetic energy when the gas begins to accelerate. As a result, the droplet always has a small temperature excess relative to the ambient gas even if the surrounding walls are at a temperature that is locally and instantaneously very close to the temperature of the droplet. This small temperature excess will then promote a rapid adjustment of the droplet to the gas temperature by evaporative cooling. Given that the gas is in equilibrium with the ice walls, the temperature of the droplet will always be very close to the local wall temperature, too, and only slowly cool as it drifts upward in the gas flow past ice walls that become colder toward the surface.

To verify the feasibility of this idea, we use results from the model in (*38*). In that model, the steady-state temperature profile of the Enceladus vents is calculated from a balance of heat supplied to the walls by condensation of vapor, conduction through the surrounding ice, and radiative loss at the south polar surface of Enceladus. An example is shown in Fig. 11. From the water table at triple-point temperature, the gas begins to flow through the channel at an initially

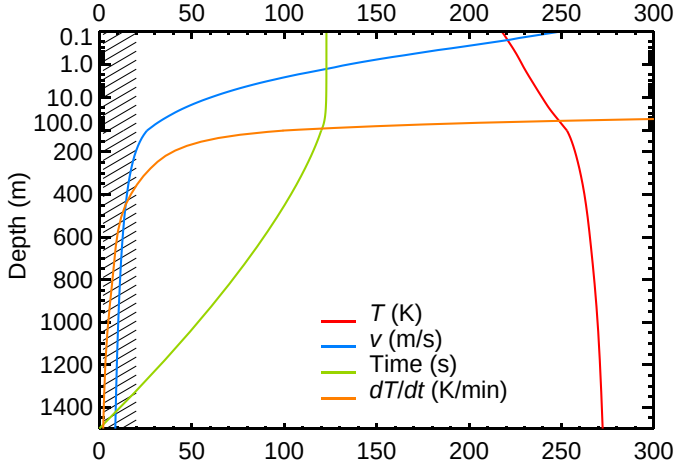


Fig. 11. Velocity, temperature, and cooling profiles in an Enceladean ice vent. Profiles of gas temperature (red) and velocity (blue) taken from an Enceladus vent model in (*38*) (corresponding to case 1 studied in the paper, shown in their figure 2). Here, the vertical coordinate is the distance along the vent, from the water table at a depth of 1500 m to the moon's surface. The unit of the horizontal axis varies for the four different plotted variables and is given in the legend. The time a Lagrangian element of the gas following the flow has spent in the channel is shown in green color. The cooling rate that this element experiences along the path is shown in orange color. The hatched region highlights the range of cooling rates (below 20 K/min, referring to the orange curve), consistent with salt segregation by freezing found in our study. The analysis in (*38*) is applied to vents of 1500 m in length from the water table to the surface, which might be a bit larger than current estimates for an about 5-km-thick ice shell (*66*–*68*) below the south polar terrain (see section S3.1 in the Supplementary Materials). However, even then, the relative change in gas velocities and temperature should be similar to the ones shown but over a shorter distance. The theoretical cooling rates for droplets entrained in the gas flow should then be respectively larger, and the total time droplets spend at slow cooling rates should be correspondingly less.

slow velocity of about 10 m/s, reaching sonic speed (above 350 m/s) and temperatures below 250 K near the outlet of the channel. The time spent by a Lagrangian gas element in the flow is also shown, calculated from the velocity profile. From that time and the temperature profile, we derived the cooling rate of the gas element ascending with the flow. This rate is initially on the order of 3 K/min and remains smaller than 20 K/min in the lowermost 75% of the channel. The associated cooling will lead to a slow freezing of the droplet from the outside to the interior, mediated by evaporation from its surface.

Evaporatively driven adjustment of droplet temperature to wall temperature is the mechanism that we propose to be responsible for the slow freezing of droplets in the order of 100 μm in size in Enceladus vents at cooling rates that are consistent with those required by our experiments for salt segregation. Because equilibration of droplets to the local wall temperatures occurs so rapidly, the effective rate of cooling is set by the speed at which a droplet is transported through the temperature gradient: slow at the bottom of the vent and much faster near the outlet into space. The initial slowness of the gas—a prerequisite for the slow cooling rates—arises naturally from the gas viscosity and friction with the vent walls.

The real cooling rates experienced by the water droplets will also depend on the three-dimensional structure of the gas flow [modeled in (*38*) as effectively one-dimensional], such as the cross-channel velocity profile, boundary layers, and the velocity slip of droplets and ice grains and the gas. For example, closer to the outlet, the vents will become narrower by vapor condensation. On the other hand, vents should become wider close to the ocean where the water table rises and falls by 10s of meters each orbit by tides [e.g., (*31*)] and ice walls are subject to erosion. Both effects will lead to even slower flows at the bottom and even faster flows near the top compared to the simple geometry used in Fig. 11. Further effects, not considered in (*38*), are homogeneous and heterogeneous condensation of supersaturated vapor in the vents, as well as a transition to supersonic speeds within the vents (*37*, *43*). Depending on the ice-to-gas mass ratio and the details of the vent profile, this could have a substantial effect, further accelerating the gas flow upstream of the trans-sonic point.

Although details of subsurface plumbing at Enceladus remain poorly constrained, the main picture follows from basic physical principles. Reference (*38*) demonstrates how the vertical temperature profile in the channels is mapped (by heat flow in the ice) to the horizontal gradient of surface temperature, which is well constrained by Cassini measurements (*42*, *44*).

Several factors not considered above may reduce the requirement for an extensive period of slow cooling before acceleration. Our estimates of evaporative cooling rates assume perfect heat transfer and no phase changes. In reality, evaporative cooling should progress more slowly because of imperfect internal heat transfer within the grains and the release of latent heat from crystallizing solid phases. However, in freezing simulations of salty droplets in environments where the vapor pressure is far from that of the droplets, these factors do not decrease the cooling rate sufficiently to achieve the rates constrained by our experiments (*45*). This means that the slow transport along a decreasing temperature gradient we propose here is required to achieve sufficiently slow cooling.

Furthermore, parent grains may not need to solidify entirely at the slower cooling rates. They need only to cool sufficiently at these rates to precipitate phosphate and carbonate salts, which should become segregated from a residual brine enriched in Na^+, K^+, and Cl^-. Because these latter species are more often observed together in CDA data, partially frozen droplets containing solid phosphates and carbonates spatially segregated from chloride-enriched brines could feasibly continue to cool more rapidly than before [for example, if ambient pressure suddenly decreases, driving enhanced rates of evaporative cooling in the upper parts of the vents (Fig. 11)] and still produce the observed subtypes. The precise temperature that must be reached by slow cooling is difficult to estimate as it is sensitive to starting concentrations of individual phosphate and carbonate species, which are also affected by pH. On the basis of our thermodynamic simulations of the fluids used for our experiments, slow cooling must be maintained until ~255 K [−18°C, where nahcolite ($NaHCO_3$) is predicted to precipitate] (Fig. 10). This is roughly consistent with the model temperature curve from Fig. 11, where the slow cooling rate <20 K/min is maintained until the gas temperature drops below 255 K. However, complete precipitation of carbonates may occur already at higher temperatures, given different starting concentrations [plausibly within the first ~5°C of cooling for high-pH fluids; (*19*, *23*)], meaning that slow cooling would only need to operate for a shorter time. In any case, minimum slow-cooling times in the order of 1 min are needed.

A two-stage freezing process where slow cooling at depth is succeeded by more rapid evaporative cooling of grains that still contain some liquid may also help explain the observed association of hydroxide anions with the chloride-bearing subtypes: The first stage involves cooling of droplets that are close to equilibrium with the surrounding gas, where the net loss of dissolved CO_2 is minimal, while the second stage, occurring after phosphate and carbonate precipitation, operates rapidly following a decrease in ambient pressure, leading to degassing of CO_2 from the residual chloride-enriched brines, and a marked local increase in pH (and OH^- concentration) within this remaining liquid.

Last, as mentioned in the "Experimental limitations" section, the spatial resolution of the analytical tools in our experiments is a little larger than the expected salt component of typical Type 3 grains, meaning that the degree of segregation observed is a lower limit. Therefore, somewhat faster cooling rates may already generate sufficient segregation at the required scale, which is not observable using current tools.

Fragmentation of large grains through wall collisions

When entrained into the gas flow, droplets as well as frozen grains are expected to experience collisions with the vent walls (*37*). This is a consequence of a substantial velocity slip that arises in a dilute gas between particles and gas, which prevents the grains from following the gas streamlines in a nonstraight channel. Typical relative gas velocities range between a few meters per second at the bottom to a few hundred meters per second near the outlet of the channel (Fig. 11) (*37*, *38*). A substantial fraction of the ice grains escapes Enceladus at speeds above the escape speed of 239 m/s to form Saturn's E ring, while the observation of supersonic jets (*43*) requires local gas speeds of at least 1000 m/s. Therefore, each frozen droplet is expected to have multiple high-speed walk collisions (*37*).

Recent impact experiments with pure crystalline ice particles (*46*–*48*) show that fragmentation for any given speed is mostly dependent on the grain size (Fig. 12). At ~100 m/s, particles of about 9 μm in diameter and larger start to fragment and will be completely shattered at a diameter larger than about 50 μm. When looking at collision speeds of 300 ms, a realistic case close to the outlet, grains start to fragment already at a diameter slightly below 1 μm. In oblique

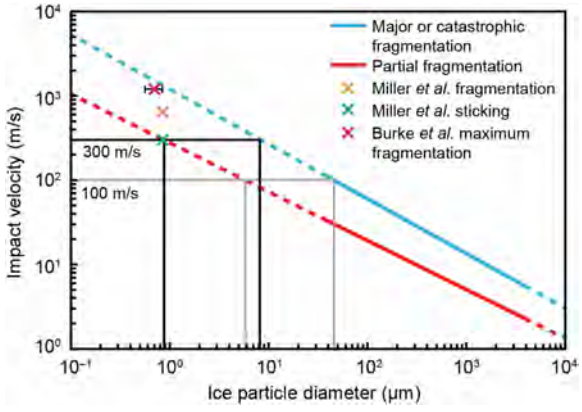


Fig. 12. Dependence of fragmentation on impact velocity and diameter of a grain before impact for pure crystalline water ice. Solid lines indicate the velocity and grain size ranges studied experimentally in (*46*); dashed lines are extrapolated from these ranges using the scaling relationships presented in that study. The red line represents the velocity above which partial fragmentation was observed in (*46*), i.e., below which no fragmentation was observed and particles just rebounded, while the dashed blue line represents the velocity above which catastrophic fragmentation was observed. The pink cross mark indicates the velocity above which no further fragmentation was observed for 0.7 (±0.14)–μm grains in (*48*). Green and orange cross marks indicate the velocities where 0.85-μm grains were observed to stick and fragment respectively in (*47*). The observed sticking case was interpreted in (*47*) as the onset of fragmentation and almost exactly agrees with the extrapolated threshold for partial fragmentation in (*46*). However, contrary to the fit presented in (*47*), the observed fragmentation case occurred somewhat lower than the extrapolated threshold for catastrophic fragmentation in (*46*). Later work in (*48*) found that the criteria for catastrophic fragmentation of 700 (+/−140 nm) ice grain particles maximized at 1200 km/s. The difference to the extrapolated values in (*46*) could be explained if the extrapolations from lower impact velocities moderately overestimate the threshold velocity for catastrophic fragmentation. In this latter case, we suggest the true threshold to lie somewhere between the observed and extrapolated impact velocities at this grain size. Two plausible cases [100 m/s (gray) and 300 m/s (black)] for impacts inside Enceladus' ice vents are indicated using the more conservative extrapolation in (*46*).

impacts, fragmentation of frozen droplets is roughly proportional to the vertical component of the impact velocity (scaling with the sine of the impact angle, e.g., for any given size, the horizontal velocity threshold would double for an impact angle of 30°), which appears to be a more realistic case in an uneven or curved channel with ledges and nozzles. However, in ice grains containing segregated salts, stresses would be concentrated at the ice-salt boundary, and these ice grains are likely to fracture at these weak points, much easier than the pure crystalline ice grains used in Fig. 12.

Even with these uncertainties resulting from the impact angle and weaker tensile strength of heterogeneous ice, it is plausible that high-velocity acceleration near the plume outlet would fragment most salt-segregated frozen droplets larger than a few micrometers and produce smaller plume particles with a compositional diversity, as observed by the Cassini CDA. The minimum size to achieve significant salt segregation lies between 15 and 100 μm in our freezing experiments, but actual sizes could be even larger. If such particles are ground down by multiple wall collisions to the sizes observed in the plume, then most of them would carry just a single salt species.

Also, in a more general sense, the sizes obtained after wall collisions fit well with the observed size distribution in the plume. The plume is dominated by micrometer particles, with grains larger than 10 μm being very rare and 50-μm particles being practically absent [(*24*, *25*); note that sizes are given there in radii, not diameter as in this work]. Collisions between ice grains inside the vents might also occur (*49*), but collision speeds would be mostly too low in this case to contribute notably to the fragmentation process. Once ejected into space, the Enceladus plume is so dilute that plume grains will practically never collide with each other.

A multicomponent plume formation process

Regardless of the specific cooling rates, our results show that segregation will not work on timescales that are allowed by a fast gas flow in an ice vent, in which ice grains would freeze in less than a couple of seconds. Freezing of Type 3 ice grains at Enceladus must occur separately from fragmentation. The requirement for slow cooling is consistent with a gas stream that initially expands slowly from the water table, maintaining a thermal quasiequilibrium with entrained droplets, ice grains, and channel walls, when flowing through channels with wall temperatures that decrease only gradually toward the surface. This implies an unexpectedly stable environment that seems at first difficult to reconcile with the requirement that grains are accelerated to fragmentation speeds in the dynamic portion of the plume that finally emerges above the moon's surface, where most grains are emitted at >100 m s^{-1} (*24*). If ice grains were accelerated to these velocities soon after formation from the ocean, they should experience rapidly changing temperatures and pressures, which would generate cooling rates incompatible with CDA observations and experimental results.

We therefore propose that—following the ejection of droplets from the ocean—the plume formation process involves at least two more stages: First, droplets freeze gradually in the lower parts of the plumbing system, where vent wall temperatures change gradually, producing segregation of individual salt species on the scale of the Type 3 grains within much larger droplets. Next, frozen droplets are accelerated by the gas flow in the upper portion of the vents leading to the surface. Within this second stage, rapid expansion of the surrounding vapor accelerates the ice grains to the required velocities for fragmentation to occur. Salt-bearing fragments inherit their water ice from the parent grains, and a thin additional ice crust might form by subsequent condensation of vapor (*9*). The observation that there is no obvious difference in grain size between the different salty subtypes (fig. S4) is consistent with such a stochastic fragmentation process. The only exceptions are the sizes of the unconstrained Na-rich subtype (Na_U)—which naturally goes down as the grain size (and, with that, signal strength) goes up—and Type 3 NaK, where salts from both alkali species appear together. The preference of the latter for larger grains could be due to the increased probability that two salt species are enclosed in the same grain if the fragment ice grains are larger.

Two aspects relevant for the Enceladus vents are not considered in the model behind Fig. 11 that will, however, facilitate an even better physical separation between the deeper, slow-moving portion of the vent system where the parent droplets freeze and the shallower, fast-moving portion where fragmentation occurs. On the one hand, erosion by oceanic tides near the bottom (*31*) could widen channels significantly there, whereas channels should preferentially narrow down by vapor condensation at the walls closer to the surface, where heat flow into the cold ice is the largest and a nozzle-type channel profile should naturally develop. In such a profile, the gas flow will become supersonic in the uppermost part of the vents, exceeding by far the gas ejection speeds of 250 to 300 m/s from Fig. 11, which are below the speeds observed by Cassini. Gas speeds above 1000 m/s

(compared to thermal/sonic speeds of 450 m/s) have been inferred from Cassini UVIS (*50*–*52*) and INMS (*53*) data for Enceladus gas jets. Furthermore, at the transition to supersonic speeds, the gas flow will reach high levels of supersaturation (*37*), leading to abundant condensation of vapor, a process not considered in the model behind Fig. 11. In part, vapor will condense on grains already entrained in the flow, but also, new ice particles can nucleate from the vapor (*37*). A fraction of the energy from the associated latent heat is transformed into kinetic energy of the gas in the vents (*37*), leading to further acceleration of the gas.

We argue that all segregated Type 3 grains must have resulted from wall collisions after droplets have frozen. However, in the deeper parts of the vents, many droplets may impact the walls before they freeze at relatively slow speeds. Although many liquid droplets will just recoil at the given slow flow conditions (*54*), some will splash, and given that the walls are at the same temperature as the droplet and even warmer below, the liquid will probably just run down the wall, eventually reentering the ocean. The lower parts of the ice walls in Enceladus vents will thus be wet.

Implications for ice grain properties ejected into the plume and the E ring

This work argues against the hypothesis in (*9*, *14*) that Type 3 ice grains directly form by flash freezing of oceanic spray. However, the ensemble of salt-rich grains together could still reliably represent the composition of the oceanic water from their parent droplets. Therefore, the approach used in (*9*) to infer the ocean composition from a coadded spectrum of all Type 3 grains analyzed at that time is still valid. One might even get more accurate results using the method applied in (*16*). There, the concentration of salts in a specific compositional subtype (Na phosphates in Type 3 Na_P) was determined and then "diluted" to oceanic concentration by dividing the phosphate concentration in the subtype by the total number of all Type 3 grains in the dataset. However, it is unclear whether the original oceanic salt–to–water ratio is maintained over multiple collisions in the fragments, even when averaged over a large ensemble. Moreover, all fragments acquire a small but unknown amount of pure water ice from vapor condensation. These effects add uncertainty to the inference of exact concentrations in the liquid from a large sample of Type 3 grains. However, the ratio of the different salts should be mostly unaffected by these processes if all salts are ejected into the plume with equal probability.

Another consequence of this work is that rare salt and organic species incorporated into oceanic parent droplets should—after fragmentation—show up only in a few grains but at relatively high concentrations. For example, the phosphate grains only constitute 9 ice grains in the analyzed dataset of 962 Type 3 grains identified in a total of more than 7300 E ring grains of all types (see the "Dataset description" section). Species at a lower concentration in the ocean than phosphates would appear in an even smaller fraction of ice grains in the plume or the E ring.

Not just Type 3 grains but practically every ice grain that formed inside the vents will be subject to high-speed wall collisions and thus fragment if too large (Fig. 12). Therefore, at least the high end of the size distribution in the Enceladean plume is determined by this fragmentation process, also applying to those grains that formed by vapor condensation (*37*) and are more numerous in the plume than salty Type 3 grains (*24*). Those fragments will not have a spherical shape, a prediction in agreement with the telescopic observations of polarization caused by the ice on the Enceladus surface (*55*) that is covered by plume material (*56*). Only grains smaller than a few micrometers at most and those forming by condensation close to the vent outlet into space will escape unaltered by wall collisions.

This process will thus also apply to organic bearing (Type 2) ice grains that are found by the CDA in a salt-poor ice matrix. These fall into two categories: initially volatile organics that are incorporated into existing ice grains by vapor condensation as the upward moving gas cools in a vent (*11*, *12*) and macromolecular organics that are already solid before cooling (*13*). These solid organics are found in a small number of ice grains at high concentrations. Reference (*13*) proposes that such refractory macromolecular organics are concentrated in an organic-enriched layer on top of the ocean, forming submicrometer-sized, probably hydrophobic aerosols after bubble bursting (much smaller than the salt-water droplets), and then serve as organic nucleation cores for water vapor, thereby forming a salt-poor icy crust before ejection into space. These grains would either survive wall collisions if they are small enough or fragment if they are too large, with both—intact and fragmented ones—ejected as ice grains mostly much smaller than 10 μm in size and indistinguishable from each other by CDA mass spectra.

Our work here now might offer an alternative scenario in which these refractory organics could originally be part of the same large saltwater parent droplets proposed earlier and then only become separated during freezing and wall collisions as described for the salts—a scenario supported by recent freezing experiments (*57*). After wall collisions, these organics would then be part of fragments containing mostly salt-poor ices from brine rejection, in agreement with the CDA analysis (*13*). However, the average salinity of these grains carrying refractory organics would be higher than in those from vapor condensates because of the residual salinity that remains in the ice after brine rejection, which is in agreement with CDA results finding slightly elevated salinities (compared to other Type 2 grains) alongside the detection of organic macromolecules (*13*).

Also, the variety of initially volatile organics that condense onto ice grains while cooling often appears chemically separated in individual grains (*11*, *12*), like the salt species reported in this work. The trace salinity of these grains of $\approx 10^{-6}$ to 10^{-7} mol/kg (*9*, *15*) is too low to stem from fragmentation of oceanic droplets. However, freezing out different organic constituents from the vapor phase at different temperatures (while gases cool on the ascent toward space) onto either salty grains or the more numerous pure water ice grains that have formed from homogeneous nucleation (*37*) could separate these organic species inside salt-poor ice grains. In case these grains grow too large, they would then become separated by fragmentation in the upper parts of the vent, similar to the salt-rich grains.

In summary, the shallow temperature gradient in Enceladus' ice vents combined with wall collisions facilitated by faster flow at shallower depths provides an efficient mechanism to chemically separate the nonwater constituents of the ocean. This is not just true for the separation of salts from organic constituents but also separation between salts and between different organics. In the plume grains, each separated compound can then be found at strongly elevated concentrations in a relatively small fraction of ice grains. This is good news for future plume sampling missions investigating Enceladus' promising habitability (*58*), provided that they can sample and analyze ice grains individually (*59*). By contrast, analyzing the bulk composition of plume ice grains would reverse the chemical separation.

METHODS

Cosmic Dust Analyzer

The CDA on the Cassini spacecraft was designed to provide in situ measurement of cosmic dust particles (of all compositions, including ice grains) in interplanetary space within a size range of 10s of nanometers up to a few micrometers (*60*). It was able to constrain the mass, composition, and—in certain cases—electric charge and impact speed of individual dust particles (*60*). Note that because of their small size, the impact speed of E ring grains cannot be directly measured by the instrument. Instead, approximations are used here (see the "Identifying Type 3 spectra" section).

The compositional analysis of CDA works on the principle of impact ionization: When a dust particle hits the Chemical Analyzer Target (CAT) in the CDA with hypervelocity ($v > 1$ km/s), it is vaporized and partially ionized because of the high internal energy density produced by the impact. Subsequently, positively and negatively charged species are separated by a strong applied electric field: Electrons and negatively charged ions are collected by the CAT, while the positively charged ions are accelerated toward a multiplier (MP) in about 23-cm distance (*60*). About 50% of these accelerated cations are collected by the so-called ion grid (QI) in front of the MP to produce a signal there. From the amplitude of the QI signal, the total ion yield can be inferred. The remaining positively charged elements and molecules are detected by the MP separated by their time of flight, thereby producing a time-of-flight mass spectrum that allows to assess the chemical composition of the dust grain. The spectrum recording can be triggered either (i) by, after impact, the collected negative charge at the target exceeding a threshold or (ii) by the burst of the first abundant cation species, such as H^+, H_3O^+, and Na^+, exceeding a signal threshold at the MP (*60*). In the latter case, the ion species that triggered the recording (and those who arrived earlier) are not part of the recorded spectrum. The recording ends after 6.4 μs, yielding 640 data points (one data point each 10 ns). Depending on the trigger that defines a starting point, this end point typically is equivalent to a maximum recorded mass of 180 to 230 u. Each time-of-flight spectrum has to be properly converted into a mass spectrum by adjusting, by hand, appropriate stretch and shift parameters, allowing to obtain the masses forming peaks at a specific time of flight. The amplitude or integral of each peak is indicative of the abundance of a certain cation mass species forming that peak.

For a more detailed description of the instrument, we refer to (*60*). More details about the spectrum acquisition and calibration can be found in (*13*, *20*), where also instrumental disturbances and contamination effects are described in more detail.

E ring CDA data analysis

Dataset description

All data used for this work are listed in Table 2 and, like all CDA data, are archived on the Small Bodies Node of the Planetary Data System (PDS-SBN) at http://sbn.psi.edu/archive/cocda. We used 15 time periods between 2004 and 2008, covering times of CDA pointing that are favorable for the detection of E ring dust. Times this early in the Cassini tour were chosen because CDA contamination from salts deposited on the CDA impact target during deep Enceladus plume crossings is then negligible (*61*). Within these periods, a total of 7353 spectra from E ring grains were recorded. A specific noise filter ("Lee filter") was applied to each spectrum to improve the SNR. Of these spectra, 961 have been categorized as Type 3.

Spectral analysis

To obtain comparable amplitudes of peaks in individual spectra, the baselines of all spectra in the dataset are corrected manually. Then, 2σ (here, σ is the standard deviation of local noise) is set as the peak significance threshold, and above that level, an ion species is classified as "detected."

Identifying Type 3 spectra

The criterion for identifying Type 3 spectra in the dataset is as follows: If the H_3O^+ (19 u) peak amplitude is lower than that of Na^+ (23 u) or K^+ (39 u), and there is at least one additional peak of a salt cluster such as Na^+(NaOH) and K^+(KCl) (as defined in the "CDA analysis of compositional variation in the population of salt-rich ice grains" section), the spectrum is classified as Type 3. However, there are two principal cases in which it is impossible to directly determine whether the H_3O^+ (19 u) peak amplitude is higher or lower than that of Na^+ (23 u) or K^+ (39 u):

1) The spectrum is recorded starting at the mass corresponding to H_3O^+ (19 u), and the spectrum therefore has likely been triggered by H_3O^+ (19 u; see the "Cosmic Dust Analyzer" section). In this case, the spectrum is only considered as Type 3 if both of the following two conditions are met: (i) There are alkali cations (e.g., Na^+ and/or K^+) present together with at least one salt cluster such as Na^+(NaOH) and K^+(KCl). (ii) No water cluster of the form $H_3O^+(H_2O)$ (37 u) is detected, because then, the invisible H_3O^+ (19 u) can be profoundly assumed to be less abundant than Na^+ (23 u) or K^+ (39 u).

2) The spectrum is recorded starting at the mass corresponding to Na^+ (23 u) or K^+ (39 u), and the spectrum therefore has likely been triggered by Na^+ (23 u) or K^+ (39 u). In this case, because a spectrum is supposed to be triggered by its first sufficiently abundant cation species reaching the MP (see the "Cosmic Dust Analyzer" section), H_3O^+ (19 u) can be safely assumed to be less abundant than Na^+ (23 u) or K^+ (39 u), respectively, because otherwise, it would have triggered the spectrum recording instead. In this case, we categorize the spectrum as Type 3 if the following condition is met: (i) At least one salt cluster as defined in the "CDA analysis of compositional variation in the population of salt-rich ice grains" section, such as Na^+(NaOH) and K^+(KCl), is present.

Distinguishing interfering species at 81 u

Both ion clusters $Na^+(Na^{35}Cl)$ (81 u) and $Na^+(NaOH)(H_2O)$ (81 u) share the same mass at 81 u indistinguishable by the CDA, and the latter species therefore could in principle lead to a false-positive detection of a chloride-rich subtype (Type 3 Na_Cl). These two species could be in principle distinguished by the presence of a cluster bearing chloride's second-most abundant isotope ^{37}Cl with an abundance ratio of $Na^+(Na^{35}Cl)$ (81 u) to $Na^+(Na^{37}Cl)$ (83 u) of 0.32. Thus, if the amplitude ratio of 83 to 81 u is about 0.3, the peak at 81 u should be almost solely due to $Na^+(Na^{35}Cl)$ (81 u); if this amplitude ratio is notably lower than 0.3, there is a contribution from $Na^+(NaOH)(H_2O)$ at 81 u. However, the method does often not work for CDA spectra because of the limited mass resolution, which is, in most cases, not reliably able to separate 81 u from 83 u.

In analog spectra with a higher resolution than CDA, such as in our laser-induced liquid beam ion desorption experiment simulating CDA spectra (*18*), these two species can be distinguished. There, we found that the presence of water cluster ions $Na^+(NaOH)(H_2O)$ at 81 u always coincides with even more abundant water cluster ions of the form $Na^+(H_2O)$ at 41 u. Such a feature at 41 u is easily observable in CDA spectra, and therefore, we only assign a feature at 81 u to be $Na^+(Na^{35}Cl)$—signifying Type 3 Na_Cl—if there is no

Table 2. CDA Type 3 spectra used for this work. The Saturn distance is given in Saturn radii (equatorial radius R_S = 60,300 km). Given that the impact speed onto the CDA cannot be measured directly for these small grains, the relative velocity of the spacecraft to a circular Kepler orbit—as an approximation for circum Saturnian dust in the E ring—provides a rough estimate. The speed range given is the range covering all individual impacts recoded during the respective observation period leading to Type 3 spectra (see the "Identifying Type 3 spectra" section). Thus, the range does not reflect the uncertainty of the speed estimate of individual impacts. We show how to estimate the speed for each individual impact in the "Identifying Type 3 spectra" section.

Period no.	Period from / to (UTC)	Period from / to (SCLK)	Total Type 3 spectra	Spectra triggered by impact	Spectra triggered by MP before Na^+	Estimated impact speed range (km/s)	Saturn radial distance (R_S)
1	2004-10-27 23:50:16 / 2004-10-28 23:25:50	1477613739 / 1477698673	39	8	31	4.5 to 6.5	6.6 to 9.3
2	2005-03-08 20:03:02 / 2005-03-10 02:41:35	1489004979 / 1489115292	94	22	55	4.9 to 8.4	3.5 to 10.1
3	2005-06-26 09:35:30 / 2005-06-26 18:40:44	1498471387 / 1498504101	45	23	40	6.2 to 8.7	3.6 to 5.5
4	2005-09-24 03:12:16 / 2005-09-25 04:59:27	1506224443 / 1506317274	78	27	68	6.4 to 9.2	5.2 to 16.6
5	2005-10-29 20:56:28 / 2005-10-30 09:02:39	1509312314 / 1509355886	122	38	97	4.2 to 7.2	4.6 to 7.6
6	2005-11-26 08:29:18 / 2005-11-26 23:31:28	1511686700 / 1511740830	51	15	37	6.5 to 7.3	8.3 to 14.5
7	2005-12-24 04:19:14 / 2005-12-25 06:50:35	1514090911 / 1514186393	120	44	102	4.2 to 7.2	4.6 to 10.6
8	2006-01-16 06:21:33 / 2006-01-18 14:44:13	1516085464 / 1516288425	16	6	14	3.8 to 6.6	5.6 to 16.2
9	2006-02-25 00:58:00 / 2006-02-26 02:10:00	1519522073 / 1519612793	193	37	121	3.8 to 6.6	5.6 to 9.9
10	2006-03-21 10:14:22 / 2006-03-22 18:02:44	1521629068 / 1521743571	89	44	82	5.6 to 6.7	9.5 to 21.0
11	2006-12-03 00:24:12 / 2006-12-03 06:33:08	1543798599 / 1543820736	34	25	31	10.0 to 12.6	4.9 to 6.8
12	2006-12-15 04:41:46 / 2006-12-15 16:59:56	1544850860 / 1544895150	4	2	3	8.2 to 8.9	4.7 to 10.3
13	2007-05-10 19:14:05 / 2007-05-10 19:59:44	1557517679 / 1557520418	34	14	24	10.3 to 10.3	4.6 to 4.8
14	2008-05-09 22:56:12 / 2008-05-10 02:19:47	1589067220 / 1589079435	39	38	39	14.3 to 14.8	4.3 to 4.7
15	2008-11-16 20:59:47 / 2008-11-16 21:25:45	1605562751 / 1605564309	3	1	3	16.2 to 16.2	4.3 to 4.3
TOTAL			**961**	**344**	**747**	**3.8 to 16.2**	**3.5 to 21.0**

peak at 41 u of comparable or larger amplitude. In all spectra categorized in this group, we have only identified no or only a small signature at 41 u and can therefore safely assume that there is only minor or no interference with a water cluster ion at 81 u.

Spectral coadding

For the CDA spectra shown in this work, coadding of a number of individual spectra is used to reduce the stochastic effects in spectral appearance resulting from variation in quality, salt concentration, and impact speed between individual ice particles of a certain subtype. In addition, spectral coadding can improve the SNR and thus can reveal additional peaks produced by potential trace substances in the ice particles. The technical details of coadding are described in section S1.2 of the Supplementary Materials.

Estimates for particle impact speed and size

Apart from the particles' compositional information, we can obtain the spacecraft location at the time of an impact event by reconstruction of the spacecraft's trajectory (*62*). However, the impact speeds of the particles corresponding to each spectrum used in this work cannot be directly measured by CDA's entrance grid system [see the "Cosmic Dust Analyzer" section and (*60*)] because of the small sizes of E ring grains. Instead, an indirect method is used to estimate the impact speeds in this work: The estimate is based on an approximation that E ring particles orbit Saturn on circular prograde orbits in the equatorial ring plane. Knowing the distance from Saturn's center at which a grain was detected, the mass of Saturn, and the speed of Cassini relative to Saturn, the impact speed can be estimated under this assumption. The error of this impact speed estimate lies in the uncertainty of the ice grains' eccentricity and inclination.

In addition, we use the presence of H^+ (1 u) as a less uncertain indicator for an impact speed threshold. Reference (*61*) could show that the presence of an H^+ peak from a water ice grain requires an impact speed of at least 10 to 11 km/s, a value later confirmed with accelerator experiments of mineral grains (*63*). Therefore, in case an H^+ peak is present or the spectrum recording has been triggered by them (see the "Cosmic Dust Analyzer" section), we assume an impact speed of at least 10 km/s regardless of the estimate from the assumption of a circular prograde orbit of the impinging ice grain described above.

The mass and size of an ice particle cannot be measured directly either. Instead, it can be estimated with an empirical equation on the basis of the ion yield and the previously estimated impact speed (*64*). Thus, the mass estimate has a very high uncertainty that can only be reduced to an acceptable level by averaging over a large number of events. On the basis of the approximations that all ice particles are spheric, and the density of these ice particles are that of pure water, the equivalent radii of ice particles used in fig. S4 are calculated.

Freezing experiments

Experimental setup

The experimental system was composed of a deep freezer (MDF-C8V1-PJ; PHC Corp.), a stainless-steel vacuum chamber (interior radius = 30 mm; height = 38 mm; interior volume = 71 mm^2; Toyo Koatsu Inc.) connected to a rotary pump with a cold trap (G-101S; ULVAC Inc.), a capacitance manometer (VG-221; HORIBA Ltd.), and a thermocouple (SAKAGUCHI E.H VOC. Corp.). Droplets of premixed solutions set in the deep freezer were frozen on a stainless-steel plate (10 mm by 10 mm) at a controlled freezing rate under air and ambient pressure. The thermocouple was attached to the stainless-steel plate to measure the temperature during the experiments. The air temperature was also measured using another thermocouple installed in the deep freezer. Both the wall and floor of the deep freezer were cooled, and the temperature difference between the plate and air was always at 2° to 2.5°C. Freezing probably begun at the boundary with the plate but then spread over the entire surface in contact with the cooled atmosphere. In one experiment (fig. S11), the metal plate was replaced with a thermally insulating glass plate as a substrate, reducing the temperature difference between the plate and the air to 0.5°C or less, which, however, severely restricted the elemental analysis (see the respective section below). The vacuum chamber set in the deep freezer was used for freeze-drying of the frozen droplets.

In addition to the freezing experiments with controlled cooling rate, flash freezing experiments were conducted through immersing droplet samples on the stainless-steel plate into liquid N_2 in the deep freezer. In flash freezing experiments, the droplets were covered with N_2 upon freezing; however, N_2 is chemically inert and would not affect the salt precipitation.

Sample preparation and procedure

We prepared starting solutions with a single composition, Na-K-Cl-HCO_3-PO_4 solution, with 374 mM Na, 25 mM K, 125 mM Cl, 100 mM $\sum CO_2$ (a sum of dissolved CO_2, HCO_3^-, and CO_3^{2-}), and 40 mM $\sum PO_4$ (a sum of PO_4^{3-}, HPO_4^{2-}, and $H_2PO_4^-$). Also, see table S7. These concentrations are based on the estimation for Enceladus' ocean (*4*, *9*, *16*). The concentrations of $\sum PO_4$ were about twice as high than the upper limit suggested for Enceladus' ocean (*16*) and aimed to better observe spatial distributions of phosphate in freeze-dried droplet samples with microscopic elemental analysis that did not appear clearly at lower concentrations.

The starting solutions were generated by mixing pure NaCl (purity >99.5%; Wako Pure Chemical Industries Ltd.), KCl (purity >99%; Kako Pure Chemical Industries Ltd.), $NaHCO_3$ and Na_2CO_3 powder (purity >99.5%; Wako Pure Chemical Industries Ltd.), and Na_3PO_4 powder (purity >96%; Sigma-Aldrich Ltd.) with ultrapure water (Milli-Q; Millipore) in precleaned propylene bottles (100 ml). The pH values of the starting solutions were measured as ~10.8 with a compact pH meter (LAQUAtwin pH-22; HORIBA Ltd.), with the electrode calibrated with buffer solutions at pH 4.01 and 6.86 (at 25°C).

After preparation of the starting solutions, droplets of the solutions with different sizes were generated on the stainless-steel plate using a micropipette (Thermo Fisher Scientific) or a nebulizer (NAVIS) for the droplet size of 15 μm. In the experiments, we varied both droplet size (approximate diameters of 1000, 200, and 15 μm) and cooling rate [−1, −5, −10, and −20 K min^{-1} and flash freezing (>1000 K min^{-1})]. Three to 10 droplets were generated on the stainless-steel plate for each experimental run. The plate was then placed in the freezer. Note that the diameter refers to the liquid state after the droplets had been put onto a plate and the shape of the droplets had flattened from an initial hemispherical droplet to the one with an aspect ratio of roughly 4:1. Therefore, the equivalent radius of a spherical droplet would be about 40% lower.

In all experimental runs, the droplets were cooled below 240 K where the solutions completely freeze. Although freezing occurs from all sides inward, the temperature gradient is not isotropic because the most efficient cooling of the droplet is applied from the bottom plate.

While staying in the deep freezer, frozen droplets were then moved to the vacuum chamber for freeze-drying while keeping the temperature of the plate at about 220 K. Then, the vacuum chamber was evacuated until complete loss of H_2O ice for at least 3 hours. The

evacuation rate was controlled to keep the structure of precipitated salts on the plate. The height of the frozen droplets shrunk during freeze-drying because of the sublimation of ice. For example, the height of freeze-dried droplets with a diameter of 200 μm and a maximum height of several 10s of micrometers typically shrunk to about 5 μm after freeze-drying. However, the diameter of the droplets did not change notably. After freeze-drying, the samples were preserved in a desiccator.

Elemental analysis

Microscopic observations and elemental analysis of the freeze-dried samples were performed with a field-emission electron probe micro analyzer (JXA-8530F; JEOL) with a nominal accelerating voltage of 10 keV. The penetration depth of an electron with an energy of 10 keV is estimated as 2 to 3 μm, assuming NaCl crystal. Elemental mapping for the freeze-dried droplets provides the sum of each elemental composition integrated from the surface to the 2- to 3-μm depth inside the droplets at a given location. The height of the droplets with a diameter of 1000 μm was ~5 to 10 μm; therefore, elemental mapping of 1000-μm-diameter droplets reflects the elemental composition of roughly the upper half of the droplets. To investigate the vertical distribution of elements within the droplet, we also changed the accelerating voltage to 5 and 15 keV, corresponding to the electron penetration depths of 0.5 to 1 μm and 3 to 4 μm, respectively. The beam size was 400 nm, which roughly corresponded to the smallest size of a plume particle of Enceladus detected by the CDA (*14*). The vacuum condition of the sample chamber for EPMA was $<1.3 \times 10^{-3}$ Pa. Elemental mapping for Na, K, Cl, C, P, and O was performed. Pure NaCl (for Na and Cl), KCl (for K), and calcite (for C and O) were used as the standard samples for quantification. The average intensities and deviations of Na, Cl, C, and O signals for five different locations on the standard samples were obtained. Using the linear relationship between the abundance and the EPMA signal intensity, Na, Cl, C, and O abundances in the samples were calculated. Through the EPMA for 5 to 10 droplets for each experiment, we obtained the elemental compositions at 10^3 to 10^4 points in total for a droplet size of 15 μm at any given cooling rate, 10^5 points for 200 μm, and more than 10^6 points for 1000 μm.

In one freezing experiment where the metal plate at the bottom was replaced by a glass plate for better thermal insulation (fig. S11), elemental mapping of alkali metals with high accuracy was obstructed because the glass also contained these elements. Moreover, carbon mapping, and with that, carbonate tracking, was entirely compromised because a thin carbon coating had to be applied on the glass substrate to provide a conductive pathway for excess electrons to dissipate to ground and prevent electrostatic charging of the sample surface.

We define Na-, Cl-, and C-rich areas in the obtained elemental map of freeze-dried droplets as a pixel with respective signal intensities of Na, Cl, and C greater than 20% of their highest intensities in the entire elemental map. As for K and P, we consider the thresholds for K- or P-rich areas as 40% of their highest intensities in an elemental map because these signal intensities were generally weak in elemental mapping and because pixels greater than 20% of the highest intensities often include pixels outside freeze-dried droplets.

Thermodynamic equilibrium calculations

We modeled equilibrium salt assemblages that form upon freezing of droplets with a composition used in the freezing experiments using the thermodynamic aqueous chemistry package PHREEQC (*27*). The package models the behavior of aqueous systems on the basis of Pitzer equations that describe ion interactions depending on composition and temperature (*65*). For our models, we used an extended version of the frezchem.dat database for subzero temperature chemistry that is available for PHREEQC (*19*). A detailed description of the database and an alike modeling approach can be found in (*19*).

For our models, we assumed an ionic composition that is equivalent to those of the freezing experiments (table S7), resulting in an HCO_3^-/CO_3^{2-} ratio of 0.14. We modeled the freezing process of droplets that are formed from room temperature (20°C) down to subzero temperatures in steps of 0.07 K. Charge balance was achieved by pH equilibration, that is, balancing H^+ and OH^- in the system for each reaction step. Equilibrium with CO_2 in the atmosphere (400 ppm) was assumed.

Supplementary Materials

This PDF file includes:

Supplementary Text
Tables S1 to S7
Figs. S1 to S13
References

REFERENCES

1. G. Choblet, G. Tobie, C. Sotin, M. Běhounková, O. Čadek, F. Postberg, O. Souček, Powering prolonged hydrothermal activity inside Enceladus. *Nat. Astron.* **1**, 841–847 (2017).
2. Y. Liao, F. Nimmo, J. A. Neufeld, Heat production and tidally driven fluid flow in the permeable core of Enceladus. *J. Geophys. Res. Planets* **125**, e2019JE006209 (2020).
3. H. W. Hsu, F. Postberg, Y. Sekine, T. Shibuya, S. Kempf, M. Horányi, A. Juhász, N. Altobelli, K. Suzuki, Y. Masaki, T. Kuwatani, S. Tachibana, S.-i. Sirono, G. Moragas-Klostermeyer, R. Srama, Ongoing hydrothermal activities within Enceladus. *Nature* **519**, 207–210 (2015).
4. J. H. Waite, C. R. Glein, R. S. Perryman, B. D. Teolis, B. A. Magee, G. Miller, J. Grimes, M. E. Perry, K. E. Miller, A. Bouquet, J. I. Lunine, T. Brockwell, S. J. Bolton, Cassini finds molecular hydrogen in the Enceladus plume: Evidence for hydrothermal processes. *Science* **356**, 155–159 (2017).
5. F. Spahn, J. Schmidt, N. Albers, M. Hörning, M. Makuch, M. Seiss, S. Kempf, R. Srama, V. Dikarev, S. Helfert, G. Moragas-Klostermeyer, A. V. Krivov, M. Sremčević, A. J. Tuzzolino, T. Economou, E. Grün, Cassini dust measurements at Enceladus and implications for the origin of the E ring. *Science* **311**, 1416–1418 (2006).
6. J. Hillier, S. F. Green, N. McBride, J. P. Schwanethal, F. Postberg, R. Srama, S. Kempf, G. Moragas-Klostermeyer, J. A. M. McDonnell, E. Grün, The composition of Saturn's E ring. *Mon. Not. R. Astron. Soc.* **377**, 1588–1596 (2007).
7. S. Kempf, U. Beckmann, G. Moragas-Klostermeyer, F. Postberg, R. Srama, T. Economou, J. Schmidt, F. Spahn, E. Grün, The E ring in the vicinity of Enceladus: I. Spatial distribution and properties of the ring particles. *Icarus* **93**, 420–437 (2008).
8. S. Kempf, M. Horányi, H.-W. Hsu, T. W. Hill, A. Juhász, H. T. Smith, "Saturn's diffuse E ring and its connection with Enceladus," in *Enceladus and the Icy Moons of Saturn*, P. M. Schenk, R. N. Clark, C. J. A. Howett, A. J. Verbiscer, J. H. Waite, Eds. (University of Arizona Press, 2018), pp. 195–210.
9. F. Postberg, S. Kempf, J. Schmidt, N. Brilliantov, A. Beinsen, B. Abel, U. Buck, R. Srama, Sodium salts in E-ring ice grains from an ocean below the surface of Enceladus. *Nature* **459**, 1098–1101 (2009).
10. F. Postberg, S. Kempf, J. K. Hillier, R. Srama, S. F. Green, N. McBride, E. Grün, The E ring in the vicinity of Enceladus II: Probing the moon's interior—The composition of E-ring particles. *Icarus* **193**, 438–454 (2008).
11. N. Khawaja, F. Postberg, J. Hillier, F. Klenner, S. Kempf, L. Nölle, R. Reviol, Z. Zou, R. Srama, Low-mass nitrogen-, oxygen-bearing, and aromatic compounds in Enceladean ice grains. *Mon. Not. R. Astron. Soc.* **489**, 5231–5243 (2019).
12. N. Khawaja, F. Postberg, T. R. O'Sullivan, M. Napoleoni, S. Kempf, F. Klenner, Y. Sekine, M. Craddock, J. Hillier, J. Simolka, L. H. Sánchez, R. Srama, Detection of organic compounds in freshly ejected ice grains from Enceladus's ocean. *Nat. Astron.* **9**, 1662–1671 (2025).
13. F. Postberg, N. Khawaja, B. Abel, G. Choblet, C. R. Glein, M. S. Gudipati, B. L. Henderson, H.-W. Hsu, S. Kempf, F. Klenner, G. Moragas-Klostermeyer, B. Magee, L. Nölle, M. Perry, R. Reviol, J. Schmidt, R. Srama, F. Stolz, G. Tobie, M. Trieloff, J. H. Waite, Macromolecular organic compounds from the depths of Enceladus. *Nature* **558**, 564–568 (2018).
14. F. Postberg, J. Schmidt, J. Hillier, S. Kempf, R. Srama, A salt-water reservoir as the source of a compositionally stratified plume on Enceladus. *Nature* **474**, 620–622 (2011).

15. F. Postberg, R. N. Clark, C. J. Hansen, A. J. Coates, C. M. Dalle Ore, F. Scipioni, M. M.Hedman, J. H. Waite, "Plume and surface composition of Enceladus," in *Enceladus and the Icy Moons of Saturn*, P. M. Schenk, R. N. Clark, C. J. A. Howett, A. J. Verbiscer, J. H. Waite, Eds. (University of Arizona Press, 2018), pp. 129–162.
16. F. Postberg, Y. Sekine, F. Klenner, C. R. Glein, Z. Zou, B. Abel, K. Furuya, J. K. Hillier, N. Khawaja, S. Kempf, L. Noelle, T. Saito, J. Schmidt, T. Shibuya, R. Srama, S. Tan, Detection of phosphates originating from Enceladus's ocean. *Nature* **618**, 489–493 (2023).
17. C. Glein, N. Truong, Phosphates reveal high pH ocean water on Enceladus. *Icarus* **441**, 116717 (2025).
18. F. Klenner, F. Postberg, J. Hillier, N. Khawaja, R. Reviol, R. Srama, B. Abel, F. Stolz, S. Kempf, Analogue spectra for impact ionization mass spectra of water ice grains obtained at different impact speeds in space. *Rapid Commun. Mass Spectrom.* **33**, 1751–1760 (2019).
19. F. Klenner, L. M. Fifer, B. Journaux, A. D. Bravenec, A. M. M. Leal, S. D. Vance, D. C. Catling, Supercooling, glass formation, and mineral assemblages upon freezing of salty ice grains from Enceladus's ocean. *Planet. Sci. J.* **6**, 65 (2025).
20. F. Postberg, S. Kempf, R. Srama, S. Green, J. Hillier, N. McBride, E. Grün, Composition of Jovian dust stream particles. *Icarus* **183**, 122–134 (2006).
21. W. Stumm, J.J. Morgan, *Aquatic Chemistry: Chemical Equilibria and Rates in Natural Waters* (John Wiley & Sons, New York, ed. 3, 1996), p. 1040.
22. K. Lodders, Solar system abundances and condensation temperatures of the elements. *Astrophys. J* **591**, 1220–1247 (2003).
23. M. G. Fox-Powell, C. R. Cousins, Partitioning of crystalline and amorphous phases during freezing of simulated Enceladus ocean fluids. *J. Geophys. Res. Planets* **126**, e2020JE006628 (2021).
24. A. Ershova, J. Schmidt, F. Postberg, N. Khawaja, L. Nölle, R. Srama, S. Kempf, B. Southworth, Modeling the Enceladus dust plume based on in situ measurements performed with the Cassini Cosmic Dust Analyzer. *Astron. Astrophys.* **689**, A114 (2024).
25. M. M. Hedman, P. D. Nicholson, M. R. Showalter, R. H. Brown, B. J. Buratti, R. N. Clark, Spectral observations of the Enceladus plume with Cassini MS. *Astrophys. J.* **693**, 1749–1762 (2009).
26. F. Chu, S. Li, C. Zhao, Y. Feng, Y. Lin, X. Wu, X. Yan, N. Miljkovic, Interfacial ice sprouting during salty water droplet freezing. *Nat. Commun.* **15**, 2249 (2024).
27. D. Parkhurst, C. Appelo, "Description of input and examples for PHREEQC version 3: A computer program for speciation, batch-reaction, one-dimensional transport, and inverse geochemical calculations" (US Geological Survey Techniques and Methods, book 6, 2013), chap. A43, p. 497.
28. J. A. Chermak, Low temperature experimental investigation of the effect of high pH Naoh solutions on the opalinus shale, Switzerland. *Clays Clay Miner.* **40**, 650–658 (1992).
29. F. Wiederschein, E. Vöhringer-Martinez, A. Beinsen, F. Postberg, J. Schmidt, R. Srama, F. Stolz, H. Grubmüller, B. Abel, Charge separation and isolation in strong water droplet impacts. *Phys. Chem. Chem. Phys.* **17**, 6858–6864 (2015).
30. C. McCarthy, R. Cooper, S. H. Kirby, K. Rieck, L. Stern, Solidification and microstructures of binary ice-I/hydrate eutectic aggregates. *Am. Mineral.* **92**, 1550–1560 (2007).
31. E. S. Kite, A. M. Rubin, Sustained eruptions on Enceladus explained by turbulent dissipation in tiger stripes. *Proc. Natl. Acad. Sci. U.S.A.* **113**, 3972–3975 (2016).
32. K. L. Mitchell, J. Rabinovitch, J. C. Scamardella, M. L. Cable, A proposed model for cryovolcanic activity on enceladus driven by volatile exsolution. *J. Geophys. Res. Planets* **129**, e2023JE007977 (2024).
33. F. Veron, Ocean spray. *Annu. Rev. Fluid Mech.* **47**, 507–538 (2015).
34. F. J. Resch, J. S. Darrozes, G. M. Afeti, Marine liquid aerosol production from bursting of air bubbles. *J. Geophys. Res.* **91**, 1019–1029 (1986).
35. S. Christiansen, M. E. Salter, E. Gorokhova, Q. T. Nguyen, M. Bilde, Sea spray aerosol formation: Laboratory results on the role of air entrainment, water temperature, and phytoplankton biomass. *Environ. Sci. Technol.* **53**, 13107–13116 (2019).
36. D. Cordier, G. Liger-Belair, D. A. Bonhommeau, T. Séon, T. Appéré, Capillary processes in extraterrestrial contexts. *J. Geophys. Res. Planets* **129**, e2023JE008248 (2024).
37. J. Schmidt, N. Brilliantov, F. Spahn, S. Kempf, Slow dust in Enceladus' plume from condensation and wall collisions in tiger stripe fractures. *Nature* **451**, 685–688 (2008).
38. A. A. Pankine, Numerical simulations of heat exchange and vapor flow in ice fractures on Enceladus. *Icarus* **401**, 115584 (2023).
39. A. Lien, Extended Jones matrix representation for the twisted nematic liquid-crystal display at oblique incidence. *Appl. Phys. Lett.* **57**, 2767–2769 (1990).
40. S. G. Warren, R. E. Brandt, Optical constants of ice from the ultraviolet to the microwave: A revised compilation. *J. Geophys. Res.* **113**, D14220 (2008).
41. P. Lamy, Interaction of interplanetary dust grains with the solar radiation field. *Astrom. Astrophys.* **35**, 197–207 (1974).
42. J. D. Goguen, B. J. Buratti, R. H. Brown, R. N. Clark, P. D. Nicholson, M. M. Hedman, R. R. Howell, C. Sotin, D. P. Cruikshank, K. H. Baines, K. J. Lawrence, J. R. Spencer, D. G. Blackburn, The temperature and width of an active fissure on Enceladus measured with Cassini VIMS during the 14 April 2012 South Pole flyover. *Icarus* **226**, 1128–1137 (2013).
43. C. J. Hansen, L. W. Esposito, A. I. F. Stewart, B. Meinke, B. Wallis, J. E. Colwell, A. R. Hendrix, K. Larsen, W. Pryor, F. Tian, Water vapour jets inside the plume of gas leaving Enceladus. *Nature* **456**, 477–479 (2008).
44. J. R. Spencer, F. Nimmo, A. P. Ingersoll, T. A. Hurford, E. S. Kite, A. R. Rhoden, J. Schmidt, C. J. A. Howett, "Plume origins and plumbing (ocean to surface)" in *Enceladus and the Icy Moons of Saturn*, P. M. Schenk, R. N. Clark, C. J. A. Howett, A. J. Verbiscer, J. H. Waite, Eds. (University of Arizona Press, Tucson, 2018), pp. 163–174.
45. A. R. Dehghani-Sanij, S. MacLachlan, G. F. Naterer, Y. S. Muzychka, R. D. Haynes, V. Enjilela, Multistage cooling and freezing of a saline spherical water droplet. *Int. J. Therm. Sci.* **147**, 106095 (2020).
46. T. Hauk, E. Bonaccurso, I. V. Roisman, C. Tropea, Ice crystal impact onto a dry solid wall. Particle fragmentation. *Proc. R. Soc. A Math. Phys. Eng. Sci.* **471**, 20150399 (2015).
47. M. Miller, S. Burke, R. Continetti, Production and impact characterization of Enceladus ice grain analogues. *ACS Earth Space Chem.* **6**, 1813–1822 (2022).
48. S. E. Burke, M. Miller, R. Continetti, Velocity dependence of submicron ice grain rebound, sticking, particle fragmentation, and impact ionization up to 2.4 km/s. *ACS Earth Space Chem.* **7**, 764–773 (2023).
49. H. Sharma, M. M. Hedman, S. Vahidinia, New insights into variations in Enceladus plume particle launch velocities from Cassini-VIMS spectral data. *Planet. Sci. J.* **4**, 108 (2023).
50. C. J. Hansen, D. E. Shemansky, L. W. Esposito, A. I. F. Stewart, B. R. Lewis, J. E. Colwell, A. R. Hendrix, R. A. West, J. H. Waite Jr., B. Teolis, B. A. Magee, The composition and structure of the Enceladus plume. *Geophys. Res. Lett.* **38**, L11202 (2011).
51. C. J. Hansen, L. W. Esposito, J. E. Colwell, A. R. Hendrix, G. Portyankina, A. I. F. Stewart, R. A. West, The composition and structure of Enceladus' plume from the complete set of Cassini UVIS occultation observations. *Icarus* **344**, 113461 (2020).
52. G. Portyankina, L. W. Esposito, K.-M. Aye, C. J. Hansen, A. Ali, Modeling the complete set of Cassini's UVIS occultation observations of Enceladus' plume. *Icarus* **383**, 114918 (2022).
53. B. D. Teolis, M. E. Perry, C. J. Hansen, J. H. Waite, C. C. Porco, J. R. Spencer, C. J. A. Howett, Enceladus plume structure and time variability: Comparison of Cassini observations. *Astrobiology* **17**, 926–940 (2017).
54. L. Xu, W. W. Zhang, S. R. Nagel, Drop splashing on a dry smooth surface. *Phys. Rev. Lett.* **94**, 184505 (2005).
55. C. D. Morello, R. A. West, M. J. Berg, Polarization analysis of Enceladus' surface. *J. Quant. Spectrosc. Radiat. Transf.* **333**, 109331 (2025).
56. B. S. Southworth, S. Kempf, J. Spitale, Surface deposition of the Enceladus plume and the zenith angle of emissions. *Icarus* **319**, 33–42 (2019).
57. T. H. Vu, C. M. Phillips-Lander, E. C. Czaplinski, M. J. Malaska, C. P. Marshall, Differential partitioning behavior of chondritic organics in Enceladus analog ices. *ACS Earth Space Chem.* **9**, 2354–2362 (2025).
58. V. Helmbrecht, F. Postberg, N. Khawaja, R. Reichelt, F. Klein, D. Grohmann, W. D. Orsi, Enceladus-like geochemistry fuels methanogenesis under extreme CO_2 limitation, *Sci. Adv.* **12**, eaei0167 (2026).
59. F. Klenner, J. Bönigk, M. Napoleoni, J. Hillier, N. Khawaja, K. Olsson-Francis, M. L. Cable, M. J. Malaska, S. Kempf, B. Abel, F. Postberg, How to identify cell material in a single ice grain emitted from Enceladus or Europa. *Sci. Adv.* **10**, eadl0849 (2024).
60. R. Srama, T. J. Ahrens, N. Altobelli, S. Auer, J. G. Bradley, M. Burton, V. V. Dikarev, T. Economou, H. Fechtig, M. Görlich, M. Grande, A. Graps, E. Grün, O. Havnes, S. Helfert, M. Horanyi, E. Igenbergs, E. K. Jessberger, T. V. Johnson, S. Kempf, A. V. Krivov, H. Krüger, A. Mocker-Ahlreep, G. Moragas-Klostermeyer, P. Lamy, M. Landgraf, D. Linkert, G. Linkert, F. Lura, J. A. M. McDonnell, D. Möhlmann, G. E. Morfill, M. Müller, M. Roy, G. Schäfer, G. Schlotzhauer, G. H. Schwehm, F. Spahn, M. Stübig, J. Svestka, V. Tschernjawski, A. J. Tuzzolino, R. Wäsch, H. A. Zook, The Cassini cosmic dust analyzer. *Space Sci. Rev.* **114**, 465–518 (2004).
61. F. Postberg, S. Kempf, D. Rost, T. Stephan, R. Srama, M. Trieloff, A. Mocker, M. Goerlich, Discriminating contamination from particle components in spectra of Cassini's dust detector CDA. *Planet. Space Sci.* **57**, 1359–1374 (2009).
62. J. Bellerose, D. Roth, Z. Tarzi, S. Wagner, "The Cassini mission: Reconstructing thirteen years of the most complex gravity-assist trajectory flown to date" in *Space Operations: Inspiring Humankind's Future*, H. Lacoste-Francis, Ed. (Springer, Cham, 2019), pp. 575–588.
63. K. Fiege, M. Hillier, R. Srama, S. Kempf, B. Abel, U. Buck, R. Postberg, R. Srama, Calibration of relative sensitivity factors for impact ionization detectors with high-velocity silicate microparticles. *Icarus* **241**, 336–345 (2014).
64. R. Srama, "Cassini-Huygens and beyond—Tools for dust astronomy," habilitation thesis, University of Stuttgart (2009).
65. K. S. Pitzer, Thermodynamics of electrolytes. I. Theoretical basis and general equations. *J. Phys. Chem.* **77**, 268–277 (1973).

66. A. Le Gall, C. Leyrat, M. A. Janssen, G. Choblet, G. Tobie, O. Bourgeois, A. Lucas, C. Sotin, C. Howett, R. Kirk, R. D. Lorenz, R. D. West, A. Stolzenbach, M. Massé, A. H. Hayes, L. Bonnefoy, G. Veyssière, F. Paganelli, Thermally anomalous features in the subsurface of Enceladus's south polar terrain. *Nat. Astron.* **1**, 0063 (2017).
67. O. Čadek, O. Souček, M. Běhounková, G. Choblet, G. Tobie, J. Hron, Long-term stability of Enceladus' uneven ice shell. *Icarus* **319**, 476–484 (2019).
68. D. J. Hemingway, T. Mittal, Enceladus's ice shell structure as a window on internal heat production. *Icarus* **332**, 111–131 (2019).
69. N. V. Brilliantov, J. Schmidt, F. Spahn, Geysers of Enceladus: Quantitative analysis of qualitative models. *Planet. Space Sci.* **56**, 1596–1606 (2008).
70. J. N. Spitale, M. D. Tigges, A. Berne, A. Rhoden, T. A. Hurford, K. D. Webster, Curtain-based maps of eruptive activity in Enceladus's south-polar terrain at 15 Cassini epochs. *Planet. Sci. J.* **6**, 67 (2025).
71. M. M. Hedman, C. M. Gosmeyer, P. D. Nicholson, C. Sotin, R. H. Brown, R. N. Clark, K. H. Baines, B. J. Buratti, M. R. Showalter, An observed correlation between plume activity and tidal stresses on Enceladus. *Nature* **500**, 182–184 (2013).
72. F. Nimmo, C. Porco, C. Mitchell, Tidally modulated eruptions on Enceladus: Cassini ISS observations and models. *Astronomical J.* **148**, 46 (2014).
73. A. Berne, M. Simons, J. T. Keane, E. J. Leonard, R. S. Park, Jet activity on Enceladus linked to tidally driven strike-slip motion along tiger stripes. *Nat. Geosci.* **17**, 385–391 (2024).
74. O. Souček, M. Běhounková, M. Lanzendörfer, G. Tobie, G. Choblet, Variations in plume activity reveal the dynamics of water-filled faults on Enceladus. *Nat. Commun.* **15**, 7405 (2024).
75. A. P. Ingersoll, A. A. Pankine, Subsurface heat transfer on Enceladus: Conditions under which melting occurs. *Icarus* **206**, 594–607 (2010).
76. C. J. A. Howett, J. R. Spencer, J. Pearl, M. Segura, High heat flow from Enceladus' south polar region measured using Cassini's composite infrared spectrometer. *J. Geophys. Res. Planets* **116**, E03003 (2011).
77. C. J. A. Howett, G. M. Miles, L. C. Quick, Constraining the mass and energy of Enceladus' dissipation systems. *Space Sci. Rev.* **221**, 56 (2025).
78. T. I. Gombosi, M. Horanyi, Time-dependent numerical modeling of dust halo formation at comets. *Astrophys. J.* **311**, 491 (1986).
79. J. Blum, Dust agglomeration. *Adv. Phys.* **55**, 881–947 (2006).
80. S. Chapman, T. G. Cowling, *The Mathematical Theory of Non-Uniform Gases* (Cambridge Univ. Press, ed. 3, 1970).

Acknowledgments
Funding: F.P., Z.Z., and F.K. were supported by the European Research Council (ERC) under the European Union's Horizon 2020 research and innovation program (ERC Consolidator Grant 724908-Habitat OASIS). Z.Z. was supported by China Scholar Ship Council grant no. 201604910894, Y.S. was supported by the Japan Society for Promotion of Science (serial numbers JP22K21344, JP24KK0075, and JP23H00144), F.K. was supported by NASA Exobiology (23-EXO23-0054) and the NASA Habitable Worlds Program (80NSSC19K0311), M.F.-P. was supported by the UK Science and Technology Facilities Council (ST/X001180/1), and N.K. was supported by the European Research Council (ERC) under the European Union's Horizon 2020 research and innovation program (ERC Consolidator Grant 101171589-AIMS). **Author contributions:** Conceptualization: F.P. and Y.S. Methodology: F.P., Z.Z., Y.S., F.K., J.S., and T.K. Data analysis: Z.Z., F.P., M.K., and M.Ç. Visualization: F.P., Y.S., F.K., M.K., J.S., M.F.-P., and M.Ç. Validation: all authors. Funding acquisition: F.P., Y.S., F.K., M..-P., and N.K. Project administration: F.P. and Y.S. Supervision: F.P. and Y.S. Writing—original draft: F.P., Z.Z., Y.S., J.S., and M.F.-P. Writing—review and editing: all authors. **Competing interests:** The authors declare that they have no competing interests. **Data, code, and materials availability:** All CDA data used for this work are listed in Table 2 and, like all CDA data, is archived on the Small Bodies Node of the Planetary Data System (PDS-SBN) at http://sbn.psi.edu/archive/cocda. The EPMA data from the freezing experiment are stored in a public repository under http://dx.doi.org/10.17169/refubium-53177. All other data and code needed to evaluate the conclusions in the paper are present in the paper and/or the Supplementary Materials.

Submitted 18 December 2025
Accepted 13 August 2026
Published 25 September 2026
10.1126/sciadv.aee7256